

2009-01-01

Characterization And Cytotoxic Assessment Of Ballistic Aerosolized Particulates For Tungsten Alloy Penetrators Interacting With Steel Targets

Brenda Ivette Machado

University of Texas at El Paso, bimachado@miners.utep.edu

Follow this and additional works at: https://digitalcommons.utep.edu/open_etd



Part of the [Materials Science and Engineering Commons](#), and the [Mechanics of Materials Commons](#)

Recommended Citation

Machado, Brenda Ivette, "Characterization And Cytotoxic Assessment Of Ballistic Aerosolized Particulates For Tungsten Alloy Penetrators Interacting With Steel Targets" (2009). *Open Access Theses & Dissertations*. 2723.
https://digitalcommons.utep.edu/open_etd/2723

This is brought to you for free and open access by DigitalCommons@UTEP. It has been accepted for inclusion in Open Access Theses & Dissertations by an authorized administrator of DigitalCommons@UTEP. For more information, please contact lweber@utep.edu.

CHARACTERIZATION AND CYTOTOXIC ASSESSMENT OF BALLISTIC
AEROSOLIZED PARTICULATES FOR TUNGSTEN ALLOY PENETRATORS
INTERACTING WITH STEEL TARGETS

BRENDA IVETTE MACHADO

Department of Metallurgical and Materials Engineering

APPROVED:

Lawrence E. Murr, Ph.D., Chair

Stephen W. Stafford, Ph.D.

Kristine M. Garza, Ph.D.

Patricia D. Witherspoon, Ph.D.

Dean of the Graduate School

Copyright ©

by

Brenda I. Machado

2009

Dedication

Dedicated with love to all my family especially to my mother Gaby

CHARACTERIZATION AND CYTOTOXIC ASSESSMENT OF BALLISTIC
AEROSOLIZED PARTICULATES FOR TUNGSTEN ALLOY PENETRATORS
INTERACTING WITH STEEL TARGETS

by

BRENDA I. MACHADO, B.S. Metallurgical and Materials Engineering

THESIS

Presented to the Faculty of the Graduate School of

The University of Texas at El Paso

in Partial Fulfillment

of the Requirements

for the Degree of

MASTER OF SCIENCE

Department of Metallurgical and Materials Engineering

THE UNIVERSITY OF TEXAS AT EL PASO

December 2009

Acknowledgements

I would like to first express my gratitude and acknowledge to my advisor and mentor Dr. Lawrence E. Murr for his commitment and dedication to this research. I would also like to thank the members of my committee, Drs. Steve W. Stafford and K. M. Garza. Special thanks to all of my friends and colleagues that provided their time and effort in helping me complete this research, especially to Sara M. Gaytan, Diana A. Ramirez, and Raquel M. Suro.

This research was supported by the U.S. Army Research Laboratory (ARL), Aberdeen Proving Ground, MD (under Contract No. W9119X-08-D0001, Amend. #0002). Special thanks to Dr. Bryan Schuster who assisted in the project as needed.

Abstract

The aerosolized particulates produced during an impact of depleted uranium munitions can potentially contaminate extensive areas around the impact sites and cause a wide spectrum of civilian and military damage. Thus materials such as WHA have been prompted for consideration.

The present research is concerned with the regular collection of aerosol particulates associated with ballistic WHA rod penetration into rolled homogeneous steel (RHA) or other related steel armor as armor plate sequences. Particulate size characterization via scanning electron microscopy (SEM) and transmission electron microscopy (TEM) along with chemical compositions via energy dispersive spectroscopy (EDS) were the focus of this research. Particulates were directly exposed to human epithelial (lung) cells in culture to assess their inflammatory and related respiratory health effects.

W-Ni-Fe and W-Ni-Co particulate samples were examined. Most SEM/EDS results showed that the propensity of the ballistic penetration-related debris and aerosol particulate mass is associated with particle aggregates $> 1 \mu\text{m}$. Nanoparticulates were easier to observe in the TEM analyses, which account for the most significant fraction of aerosol particulate. Aerosol nanoparticulates for the majority of filter collections exhibited significant cytotoxicity for A549 human epithelial cells.

Table of Contents

Acknowledgements	v
Abstract.....	vi
Table of Contents	vii
List of Tables	ix
List of Figures	xi
Chapter 1: Introduction.....	1
1.1 Tungsten vs. Depleted Uranium.....	1
1.2 Research Objectives.....	2
Chapter 2: Background	3
2.1 Ballistic Particulates.....	4
2.2 Kinetic Energy Penetrators.....	7
Chapter 3: Experimental Procedures.....	8
3.1 Particulates.....	10
3.2 Optical Metallography.....	12
3.3 Scanning Electron Microscopy (SEM).....	13
3.4 Transmission Electron Microscopy (TEM).....	13
3.5 <i>In-vitro</i> Cytotoxicity Assessment.....	14

Chapter 4: Results and Discussion.....	16
4.1 Particulate Analysis.....	16
4.2 Microstructural Analysis.....	18
4.3 Particulate Characterization by SEM/EDS Results.....	21
4.4 Particulate Characterization by TEM/EDS Results.....	34
4.5 Cytotoxicity Results and Comparison with other Nanoparticulate Assays.....	49
Chapter 5: Summary and Conclusions.....	56
5.1 Summary.....	56
5.2 Specific Conclusions.....	57
References.....	59
Curriculum Vita.....	60

List of Tables

Table 4.1.1: Particulate Collection for 93%W-5.6%Ni-1.4%Fe (WHA) Penetrator Impact Experiment.....	17
Table 4.1.2: Particulate Collection for 91%W-6%Ni-3%Co (WHA) Penetrator Impact Experiment.....	18

List of Figures

Figure 2.1.1: Schematic view of rod and target impact at initial conditions, during and after penetration.....	5
Figure 2.1.2: X-ray image from a simulated rod penetrating into a Cu target plate.....	6
Figure 2.1.3: Micrograph composite of a residual single crystal W rod in a RHA target.....	7
Figure 2.2.1: Typical KE 120mm APFSDS-Tcartridge (sabot round) showing the complete assembly.....	9
Figure 3.1.1: Schematic view of particle collector showing the steel plates as well as the location of the filters.....	11
Figure 3.2.1: Macroscopic view of a long-rod penetrator.....	12
Figure 4.2.1: Metallographic photographs showing the W particles as well as the Ni-Fe matrix. Original magnifications: 20X, 50X, and 100X respectively. Etchant: Nital.....	19
Figure 4.2.2: Representative Microstructural features for W-Ni-Co alloy consisting of nearly spherical W particles. Original magnifications: 10X, 20X, and 50X respectively. Etchant: Nital.....	20
Figure 4.2.3: Microstructure illustrates the accommodation of a heavily deformed region in a WHA penetrator rod.....	21
Figure 4.3.1: (Top) Image showing particulate aggregates from a W-Ni-Fe firing. Original magnification: 5.0kx. (Bottom) EDAX spectrum collected on the same area as image above.....	22

Figure 4.3.2: (Top) Shows particles in another region of stage 6 ranging from 1 μm to 2 μm . (Bottom) Higher magnification view of the particle on the bottom left of the above image. Original magnifications: 25.0kx and 50.0kx respectively.....	23
Figure 4.3.3: Illustrates particles that look more agglomerated than the particles in Figure 4.3.2. Original magnification: 5.0kx.....	24
Figure 4.3.4: (Top) This image shows an agglomerated region of particles similar to Figure 4.3.3 at the same magnification. (Bottom) EDS spectrum for this area revealed a high Al peak.....	25
Figure 4.3.5: Both images show particles for both alloys on the filter at 7.0kx and 15.0kx.....	26
Figure 4.3.6: Illustrates particles smaller than 0.5 μm at an original magnification of 40.0kx.....	27
Figure 4.3.7: EDS spectrum for Figure 4.3.6 showing oxygen as the dominant peak, as well as some Fe, Al and W contents.....	28
Figure 4.3.8: This image represents an area of two particles that range from 500 nm to 750 nm. Original magnification: 80.0kx.....	28
Figure 4.3.9: Image from shot #10 also for the W-Ni-Fe projectile firings showing particles approximate to 0.1 μm . Original magnification: 50.0kx.....	29
Figure 4.3.10: (Top) EDS spectrum from a point analysis showing a small potassium peak. (Bottom) The quantification results for the EDS spectrum shows dominance of the Fe over all the percentage.....	30

Figure 4.3.11: (Top) SEM image of a small area in shot #11. (Bottom) Shot #13 image shows a large individual particle. Original magnifications: 70.0kx and 50.0kx respectively.....	32
Figure 4.3.12: (Top) EDS spectrum for shot #11 with its respective quantification results. (Bottom) EDS spectrum for shot #13 showing Fe as the major weight percent.....	33
Figure 4.4.1a: Bright-field image of the aggregate at an original magnification of 53.8kx....	34
Figure 4.4.1b: Image shows the selected-area electron diffraction pattern.....	35
Figure 4.4.1c: Dark-field image on the same area as Figure 4.4.1a.....	35
Figure 4.4.2: (Top) Area showing different sizes of particles. Original magnification: 84.3kx. (Bottom) This image shows the diffraction pattern showing only a few spots.....	36
Figure 4.4.3a: Particle aggregate for W-Ni-Co projectile firing. Original magnification: 54.4kx.....	37
Figure 4.4.3b: SAED pattern showing different spots from the different crystalline particles.....	38
Figure 4.4.3c: Image represents dark-field of the image in Figure 4.4.3a. Original magnification: 54.4kx.....	38
Figure 4.4.4: Bright-field image of different size aerosol particulates with its respective SAED pattern. Original magnification: 42.4kx.....	39
Figure 4.4.5: Bright-field image of wide distribution of crystalline aerosol particulates at a lower magnification than Figure 4.4.4.....	40
Figure 4.4.6a: Bright-field image of particulate aggregates. Original magnification: 30.0kx.....	41
Figure 4.4.6b: SAED pattern with a diffuse background.....	41

Figure 4.4.6c: Dark-field image using the diffraction spot in Figure 4.4.6b. Original magnification: 30.0kx.....	42
Figure 4.4.7: Image in bright-field showing a black halo around the big particle. Original magnification: 20.0kx.....	43
Figure 4.4.8: (Top) Image representing the same area as Figure 4.4.7 after beam charging. (Bottom) Image shows a higher magnification view of the dendritic structure. Original magnifications; 30.0kx and 40.0kx.....	44
Figure 4.4.9a: Image of a W-Ni-Fe rod penetration aggregate. Original magnification: 20.0kx.....	46
Figure 4.4.9b: EDS spectrum corresponding to Figure 4.4.9a showing a small Ni peak as well as the Cu peak from the TEM grid.....	47
Figure 4.4.10a: Bright-field image of a W-Ni-Co projectile firing. Original magnification: 20.0kx.....	47
Figure 4.4.10b: EDS spectrum showing a Co peak as well as Si and Mo peaks.....	48
Figure 4.5.1: 48 hrs cytotoxicity results for the single-stage penetration filters in culture assays.....	50
Figure 4.5.2: Cell viability assay for the Mylar filters (Event 3 and 5).....	51
Figure 4.5.3: Cytotoxicity assay results for manufactured nanoparticulate aggregate materials [15].....	52
Figure 4.5.4: Direct contact cytotoxicity assay results for human epithelial cell cultures (48 hrs) [13].....	52
Figure 4.5.5: Cytokine release for two single-stage filters (shots #11 and #3).....	53
Figure 4.5.6: IL-8 results for the same shots as in Figure 4.5.5.....	54

Chapter 1

Introduction

1.1 Tungsten vs. Depleted Uranium

The use of depleted uranium (DU) munitions especially in kinetic energy (KE) rod projectiles has been historically associated with potential long-term health issues. The aerosolized particulates produced during an impact of depleted uranium munitions can potentially contaminate extensive areas around the impact sites and cause a wide spectrum of civilian and military health concerns. This can range from lethality to inhalation or ingestion-induced adverse health effects depending upon the range of fragment sizes or size distribution [1-3]. Furthermore, Guillmette et al. [4] have also discussed the health risks associated with DU aerosols such as chronic obstructive pulmonary disease (COPD). These and other related health concerns over the use of DU munitions have prompted the consideration of alternative ballistic materials such as tungsten-heavy alloys (WHA). Kinetic energy rod projectiles made with tungsten alloys have historically been assumed to be relatively benign and to pose no health or environmental risks [5].

The assumption is based on the idea that the tungsten constituent of the alloy is non-toxic. A potential concern arises due to the presence of two toxic metals in the alloy, nickel and cobalt. Although they are in relatively small proportions, their presence raises a dilemma about risks associated with the inhalation and the ingestion of these metals. It is now well-known that ultra-fine or nanoparticulate size materials that are characterized from an extensive compositional range and particulate morphologies exhibit respiratory

inflammatory and cytotoxic effects for a collection of human lung cell types [6-12]. In the case of very small fragments and fragment aerosols, there have been very few studies concerning particulate chemistries, size distributions or cytotoxic responses that are pertinent to respiratory inflammatory responses or additional serious respiratory health effect indicators. There is a recent study by Gold et al. [13] that has examined aerosols inside an armored vehicle penetrated by a KE rod penetrator and they concluded that the aerosol data they obtained serves as a quantitative foundation for future work in the area of health-risk assessments by eliminating some of the uncertainty surrounding possible exposures to aerosols during combat. However, for embedded WHA (W-Ni-Co and W-Ni-Fe) fragment simulations using pellet samples, corrosion-related observations have correlated with *in-vivo* toxicity measurements. Different toxic effects were identified for these WHA alloys, with W-Ni-Co having a more toxic effect [14-15]. In a recent report describing sarcoma in rats implanted with the same WHA, W-Ni-Co and W-Ni-Fe, also using simulated pellet fragments have raised fear for the potential health effects these alloys can provide [15].

1.2 Research Objectives

The present research is concerned with the systematic collection of aerosol particulates associated with ballistic WHA rod penetration into rolled homogeneous steel (RHA) or other related steel armor such as armor plate sequences. The focus of this research was to characterize the size of the collected particulates using scanning electron microscopy (SEM) and transmission electron microscopy (TEM). Another focal point of this research was to analyze the particulate chemistries or elemental compositions utilizing

energy dispersive x-ray spectroscopy (EDS). Lastly, filter-collected aerosol particulates were directly exposed to human epithelial (lung) cells in culture to assess their potential inflammatory and related respiratory health effects. This work is in collaboration with the Army Research Laboratory (ARL) in Aberdeen, MD as well as the Biological Sciences Department at the University of Texas at El Paso (UTEP).

Chapter 2

Background

2.1 Ballistic Particulates

There have been only a small number of systematic collections of ballistic particulate, also known as aerosol debris, which will identify the contribution of nanoparticles and micron-size particulate chemistries [6]. This is true for KE rod penetration through thick metal or alloy targets where both target and rod erosion produced aerosol debris outflow from the entrance side of the target, concluded by the formation of a rear debris field when the projectile exits the target upon perforation as shown in Fig. 2.1.1 [16-22]. Figure 2.1.1 shows a representative view of a KE rod penetrating a target plate and the direction of a rod erosion tube (RET), target erosion tube (TET), as well as a debris field created as the projectile emerges at the rear surface of the target [23]. Fig. 2.1.2 illustrates a flash x-ray image for a simulated WHA rod, with a composition of 93% W-5% Fe, 2% Ni, perforating a 3.5 cm thick copper target plate at an impact velocity of 1.5 km/s [24]. The image illustrates the particulate debris at the entrance surface and the rear-surface debris field as the projectile exits the target. The mushrooming of the projectile surface and its erosion are visible at the exit (or rear) surface of the target plate. Additionally, Figure 2.1.2 shows that a significant fraction of debris contains larger particles roughly in the size range from <1 mm to \approx 1 cm.

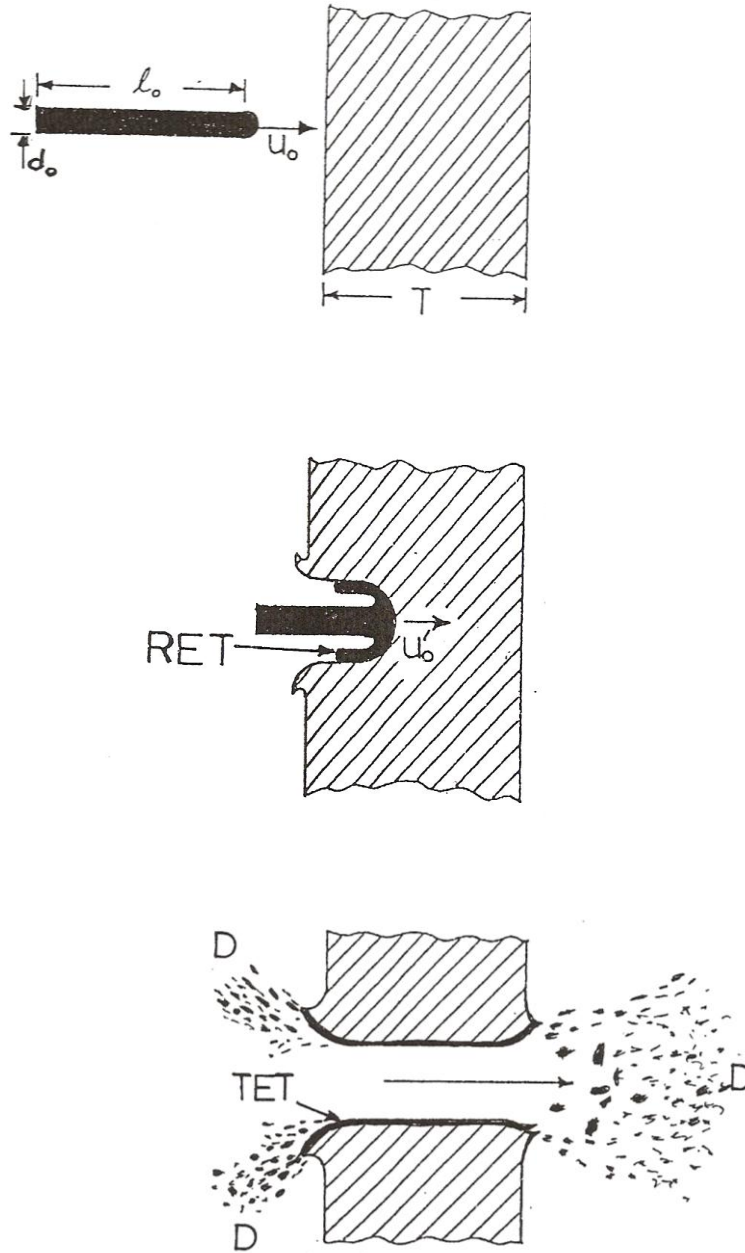


Figure 2.1.1: Schematic view of rod and target impact at initial conditions, during, and after penetration [23].

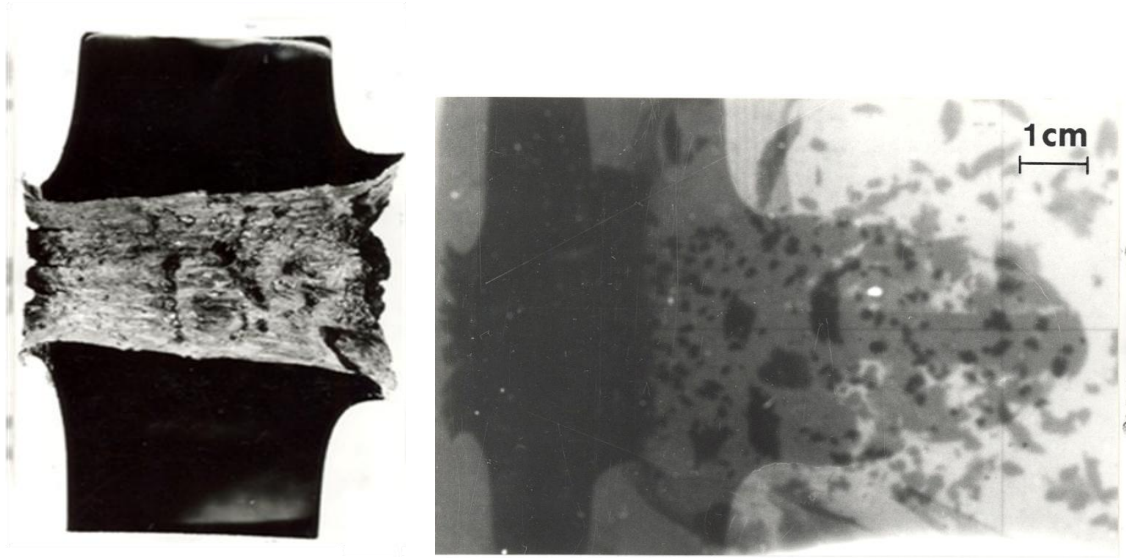


Figure 2.1.2: X-ray image from a simulated rod penetrating into a Cu target plate [24].

Both the target and the projectile erode by dynamic recrystallization (DRX) which facilitates material flow in the solid state. This produces polycrystalline, millimeter, micron and submicron-size erosion and debris fragments from both the penetrating rod and the penetrated target, including some mechanical mixing and reaction product debris between the target and the projectile [19]. Figure 2.1.3 demonstrates these erosion phenomena for a single-crystal W rod penetrating a rolled homogenous alloy armor (RHA) steel target at an impact velocity of 1.35 km/s. The projectile erosion by DRX creates a rod erosion tube (RET) that is ejected from the rear of the projectile and a target erosion tube (TET) ejected in the same direction forming the target crater rim and the related debris particulates [25]. There is a possibility of a reaction or interaction between the projectile and the target as mentioned above, and there may also be some local melt and solidification phenomena [20].



Figure 2.1.3: Micrograph composite of a residual single crystal W rod in RHA target [19].

2.2 Kinetic Energy Penetrators

The primary usage of kinetic energy penetrators (KEP) is to penetrate tank armor or any other heavily armored military vehicle. KE projectiles fired from high pressure cannons are the main armament of all modern-day battle tanks [25]. KEPs are projectile weapons that do not explode, but rather damage their target by slamming into it at high

speeds ($\approx 1.4 - 1.9$ km/sec) through the use of kinetic energy from high pressure gases that are generated by the burning of propellant in a barrel rather than from an explosive source [25]. At such velocities the trajectories are flat and the time it takes to reach the target is very short [26]. Also, it relies on mass (density) to effectively pierce the armor and destroy the target. Effective penetrators have densities noticeably greater than the target.

In the military, the term armor-piercing, fin-stabilized discarding sabot (APFSDS) is used for the most common form of KE penetrator (refer to Figure 2.2.4). This projectile has a higher length to diameter ratio; therefore it is referred to as “long rod penetrator”. It is composed of two assemblies, a combustible case and propellant assembly, and the sabot and sub-caliber projectile assembly [19]. The propellant and fuse assembly supplies the kinetic energy to the sabot and sub-caliber projectile assembly. The sabot seals the space between the barrel lining and the projectile (long-rod) (Army Products). When the projectile assembly is ejected from the barrel the high drag pulls the sabot quickly away from the long rod projectile, thereby allowing for a straight trajectory stabilizing the projectile. As mentioned before, when the projectile reaches the target, it does not explode but relies on density (mass) and velocity to achieve the necessary force to effectively pierce the armor and eventually destroy the target.



Figure 2.2.1: Typical KE 120mm APFSDS-Tcartridge (sabot round) showing the complete assembly [19].

Chapter 3

Experimental Procedures

3.1 Particulate Sampling

The ballistic aerosol/particulate sampling was accomplished using either a single-stage filter collector or an eight-stage cascade impactor. The single-stage filter is 1.2 μm in thickness and 2.5 cm in diameter. The eight-stage cascade impactor as well as the single-stage filter is connected to an RHA cube of 0.6 m on each side. Inside the cube there is a stack of 10 mild steel target plates spaced 0.5 inches (1.27 cm) from each other. Each steel plate is 0.25 inches (0.625 cm) in thickness. A schematic view is shown in Figure 3.1.1 that represents the arrangement that was employed at Range 110 at the Army Research Laboratory area of Aberdeen proving Ground, MD. It shows the filters position as well as the direction of the steel target plates. The samples analyzed were from a series of tests consisting of different shots at Aberdeen Testing Center representing the two WHAs. Four different shots were received and analyzed from the single-stage collector filter, #3 and #10 of the alloy W-Ni-Fe and #11 and #13 of the alloy W-Ni-Co. From the eight-stage cascade impactor filters two events or projectile firings were received, #3 and #5 from W-Ni-Fe and W-Ni-Co respectively. Consequently, a total of 6 ballistic events were examined in this study or three for each projectile composition: W-Ni-Fe and W-Ni-Co.

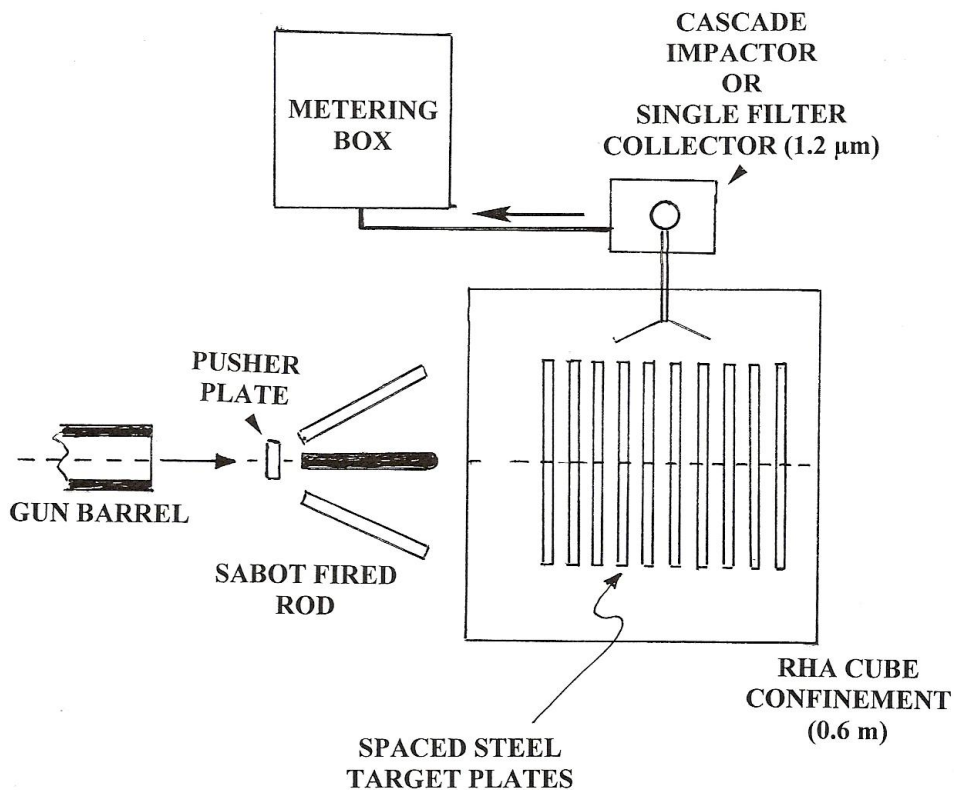


Figure 3.1.1: Schematic view of particle collector showing the steel plates as well as the location of the filters.

The debris generated by rod impact and penetration of the target plates was sampled for ≈ 15 min. at an air flow rate of 2L/min. The single-stage collector filters were preloaded, mixed cellular ester (MCE) sampling filter cassettes. For the eight-stage cascade impactor or Mylar filters, they were sprayed with Dow Corning 316 Silicone release lubricant for ≈ 16 hrs before initial weighing to provide an adhesive surface for the airborne particulates. The concentration and percentage of total weight were calculated to determine the proportion of respirable particulates. Air sample collection of analysis was conducted following National Institute for Occupational Safety and Health (NIOSH) method 7074 which included cellulose ester filter collection, acid digestion, and analysis by

inductively coupled plasma (ICP) spectroscopy. EPA method 200.7 was used for metal analysis.

3.2 Optical Metallography

Two simulated WHA long-rod penetrators used in the tests were received with two different compositions. One of the compositions was 91% W, 6% Ni, 3% Co and the other was 93% W, 7% NiFe. These rods were fabricated by powder metallurgy (PM) processing of tungsten particles in the alloy matrix and were 12 cm in length (0.6 cm diameter), with a length-to-diameter ratio of 20:1, and weighed $\approx 65\text{g}$ (refer to Figure 3.21). The impact velocity was $\approx 1.2\text{ km/s}$ with complete penetration of the projectile through the target-plate group. A small section from each rod was cut, mounted, ground, polished (using a final polish with $0.05\text{ }\mu\text{m}$ alumina), and etched using a solution of 45 mL HNO_3 and 5 mL methyl alcohol (CH_3OH) or also known as Nital. The samples were etched with a minimal exposure to the etchant of $\approx 2\text{s}$. The etched sample was quickly washed in ethanol to remove the residual etchant. The samples then were observed using a Reichert MEF4 A/M optical metallograph at different magnifications utilizing a digital image converter.

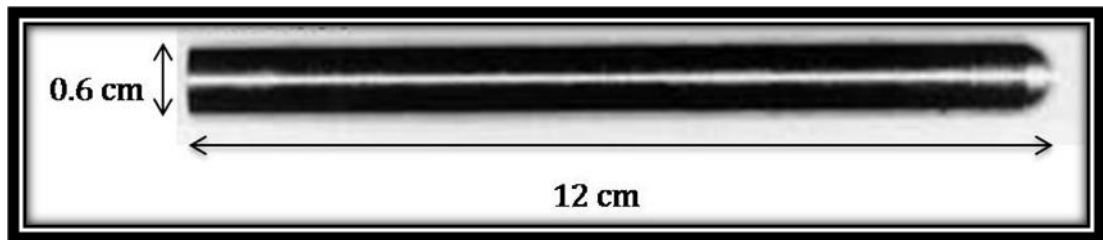


Figure 3.2.1: Macroscopic view of a long-rod penetrator [22].

3.3 Scanning Electron Microscopy

Filter collection samples from both the single-stage and cascade impactor filters were sectioned in halves or quarts for observation and analysis by scanning electron microscopy (SEM) and energy dispersive x-ray spectrometer (EDS). Specimens were coated with gold in a Gatan Precision Etching Coating System (Model 682) previous to examination. Coating was done to enhance sample conductivity and to avoid charging of the samples. Samples from the Mylar filters were coated, as well as some of the single-stage filters. The single (MCE) filter collectors were easier to be observed by scraping particles off the filter and setting them onto sticky carbon tape. The SEM used was a Hitachi S4800 operated at 15-20kv accelerating potential to assure adequate excitation for EDS.

3.4 Transmission Electron Microscopy

Direct particulate observation was completed by transmission electron microscopy (TEM). Filter sections were scraped onto silicon monoxide/formvar-coated 200 mesh, 3 mm copper grids and a second grid placed on top to form a sandwich. TEM image analysis was performed in either a Hitachi H-8000 electron microscope operated at 200 kV and fitted with a goniometer-tilt stage or a high-resolution TEM (Hitachi H-9500) operating at 300kV for ultra-fine particle (nanoparticulate) analysis. This TEM has built-in an EDAX-EDS system which allowed for nano-probe (point) analysis. Selected-area electron diffraction (SAED) was utilized to observe the degree of crystallinity of the collected particulates and to allow for selective dark-field (DF) imaging utilizing specific diffraction spots.

3.5 *In-vitro* Cytotoxicity Assessment

In this study we utilized direct contact cytotoxicity studies for filter-collected ballistic particulates as described previously by Soto et al. [10]. These studies measure *in-vitro* cell viability or cell death using colorimetric or optical densitometry analysis along with cytokine enzyme linked immune sorbent assay (ELISA) studies, which measure the up-regulation and release of interleukins by the cells. As in many cytotoxicity studies, we utilized the well-known A549 human epithelial lung cell line which provides an effective *in-vitro* lung cell model. In the A549 cell culture models as well as in bronchial alveolar lavage fluids in animals [27-32] there are two markers for inflammatory response, Interleukin 6 (IL-6) and Interleukin (IL-8) [27-32]. These two cytokines provide a biomarker link between *in-vitro* and *in-vivo* studies. Particularly, IL-6 has been associated with allergic responses involving asthma [29-32]. IL-8 has been linked with chronic obstructive pulmonary disease (COPD) [4, 31-33].

The A549 cells were cultured in 12-well plates at 0.25×10^6 cells per well in F-12 Ham's media with 10% Fetal Bovine Serum (FBS) and 5% Penicillin (PS). The cells were first cultured for several hours to allow cell adhesion and were then exposed for 48 hrs to a quarter of the indicated filter with the particulate collection facing towards the monolayer of cells. Media-treated cells or untreated cells served as the negative control. Cells were also exposed to a filter on which nothing had been collected and served as the blank control. Following the exposure period, the filters were removed; the cells were harvested, and were then transferred into a 96-well flat bottom plate to assess viability via the MTS Assay. This colorimetric assay evaluates relative viability as a function of color, which is

directly proportional to the amount of cells available to convert the substrate into a color product. CellTiter 96 Aqueous One Solution Reagent (Promega), which contains the tetrazolium compound 3-(4, 5-dimethylthiazol-2-yl)-5-(3-carboxymethoxyphenyl)-2-(4-sulfophenyl)-2H-tetrazolium, inner salt (MTS), was added to each well. The plate was then incubated for 2 hrs at 37°C in a 5% CO₂ humidified atmosphere. As a final point, the absorbance was recorded at 490 nm using a 96-well plate spectrophotometer reader.

The secretion of IL-6 and IL-8 by A549 cells was measured using a commercial human IL-6 and IL-8 enzyme-linked immunosorbent assay (ELISA) kit (Biosource Human IL-6/IL-8 CytoSet). Supernatants were obtained 48 hrs after exposure to the different filters and were stored at -20°C frozen for ELISA analysis following the manufacturer's protocol. The ELISA plates were coated 12 to 18 hrs at 4°C with the capture antibody (Anti-Human IL-6 or IL-8). The plates were then blocked at room temperature with assay buffer for 1 hr. to prevent non-specific antigen binding. After that, the standards (Recombinant Human IL-6 or IL-8) and samples were added in duplicate, immediately followed by the addition of the working detection antibody (Anti-Human IL-6 or IL-8 Biotin) and incubated for 2 hrs at room temperature. Subsequently, the plates were washed and the working streptavidin-horseradish peroxidase (HRP) solution was added to each well for 30 min. The enzyme substrate solution tetramethylbenzidine (TMB) was added for color development. The enzyme reaction was then stopped by adding the stop solution containing hydrosulfuric acid (H₂SO₄). Absorbance was measured at 450 nm using a 96-well plate spectrophotometer reader.

Chapter 4

Results and Discussion

4.1 Particulate Analysis

The rod penetration test system applied for this experiment shown in Figure 3.1.1 involves the penetration and perforation of thinner target plates in comparison to Figure 2.1.1 which involves a thick target plate. The reason behind this setting was that for multiple, spaced target plates, the erosion-created particulates from both the projectile and the target would be created more consistently allowing for a more efficient and representative sampling. Both Tables 4.1.1 and 4.1.2 demonstrate representative sampling data for WHA rod penetration of the target plates for 93%W-5.6%Ni, 1.4%Fe and 91%W-6% Ni, 3% Co (weight percents) respectively. These particulate results are specifically from the Mylar (cascade impactor collection) filters. Specific information from single-stage filters was not provided.

Table 4.1.1 reflects the total particulate concentration which represents a main contribution from the Fe in the steel target plates. The total Fe concentration in mg/m³ is two times larger than the nominal Fe content for the WHA rod projectile, in which 80% was consumed in perforating the 10 plates. Consequently, the principal Fe contribution comes from the target erosion. The respirable particulates Fe-containing particulates, $\leq 2 \mu\text{m}$ in size, are a factor of roughly 17 times the combined Ni and W concentrations (refer to Table 4.1.1). This table also illustrates that the Fe concentration for 0.9 μm cut point is approximately 10 times the combined W and Ni concentrations. A difference is observed at

0.25 and 0.5 μm cut points, where the Fe concentration is about 2 times greater than the W concentration.

Table 4.1.1: Particulate Collection for 93%W-5.6%Ni-1.4%Fe (WHA) Penetrator Impact Experiment

Stage	Cut Point (μm)	Total Particulate Weight (mg)	Total Particulate Concentration (mg/m^3)	Iron Conc. (mg/m^3)	Nickel Conc. (mg/m^3)	Tungsten Conc. (mg/m^3)
1	21	0.432	17	14.8 ^{1,2}	0.286	1.92
2	15	0.052	2	4.51 ^{1,2}	0.134	1.36
3	10	0.000	0	3.52 ^{1,2}	ND	0.217
4	6	0.049	2	7.31 ^{1,2}	0.118	0.318
5	3.5	0.798	31	21.0 ^{1,2}	0.312	0.736
6	2	0.953	38	20.9 ^{1,2}	0.29	0.781
7	0.9	0.677	27	9.97 ^{1,2}	0.412	0.625
8	0.5	0.204	8	2.25 ^{1,2}	ND	0.401
Backup Filter	0.25	0.878	35	4.89 ^{1,2}	ND	2.59
Total			160	89.2	1.28	8.95
Respirable			106	65	0.862	3.08

ND-Concentration below instrument detection limit

¹ Result is an estimated concentration

² Analyte is found in the associated blank as well as in the sample

Table 4.1.2 shows particulate collection data for the W-Ni-Co rod penetrators. The Co concentration was not detected for the first cut points. The respirable particulates are represented by the Fe-containing particulates that are similar to Table 4.1.1 for the W-Ni-Fe rod penetrators. The ratio of respirable particulates ($\leq 2 \mu\text{m}$) to the total particulate concentration is basically the same for Table 4.1.1 and 4.1.2, $\approx 66\%$ and 69% respectively. Likewise, for the W and Ni particulates in the respirable range, the ratio is essentially the same for the W-Ni-Fe collection in Table 4.1.1 as well as for the W-Ni-Co collection in Table 4.1.2. The involvement for the ballistic impact test for particulate or aerosol by projectile-target erosion that is represented in these two tables is for the respirable particulates that

are less than 2 μm . Almost, 61% of the respirable particulate concentration would originate from the steel target in the case of the W-Ni-Fe projectile penetration. In the case of the W-Ni-Co projectile penetration, the steel target contribution is $\approx 65\%$ or the same as Table 4.1.1.

Table 4.1.2: Particulate Collection for 91% W-6%Ni-3% Co (WHA) Penetrator Impact Experiment

Stage	Cut Point (μm)	Total Particulate Weight (mg)	Total Particulate Concentration (mg/m^3)	Cobalt Conc. (mg/m^3)	Nickel Conc. (mg/m^3)	Tungsten Conc. (mg/m^3)
1	21	0.216	6	ND	0.114	0.274
2	15	0.000	0	ND	ND	0.102
3	10	0.254	7	ND	ND	0.106
4	6	0.030	1	ND	0.076	0.185
5	3.5	0.841	22	0.088	0.208	0.535
6	2	0.981	26	0.068	0.174	0.580
7	0.9	0.592	16	0.184*	0.079*	0.125*
8	0.5	0.310	8	0.075	ND	0.417
Backup Filter	0.25	1.131	30	ND	0.090	1.380
Total			116	0.415	0.741	3.700
Respirable			80	0.415	0.537	1.950

ND-Concentration below instrument detection limit

*Sample was filtered

4.2 Microstructural Analysis

Metallographic evaluation was performed on the WHA rods with the same dimensions as the one shown in Figure 3.2.1 to confirm the microstructure. The following microstructures are representative of the alloys W-Ni-Fe and W-Ni-Co respectively. Figure 4.2.1 illustrates the cross-section microstructures for W-Ni-Fe test projectile at different magnifications. The examination revealed W particles that are nearly spherical in a Ni-Fe matrix. Figure 4.2.2 shows W particles almost circular in shape, a typical microstructure for W-Ni-Co, but now in a Ni-Co matrix. Murr et al. [18-22] have shown deformation of

WHA penetrator rods (refer to Figure 4.2.3). This figure shows a microstructure from an embedded penetrator in a RHA steel target. The deformation can be observed in the microstructure.

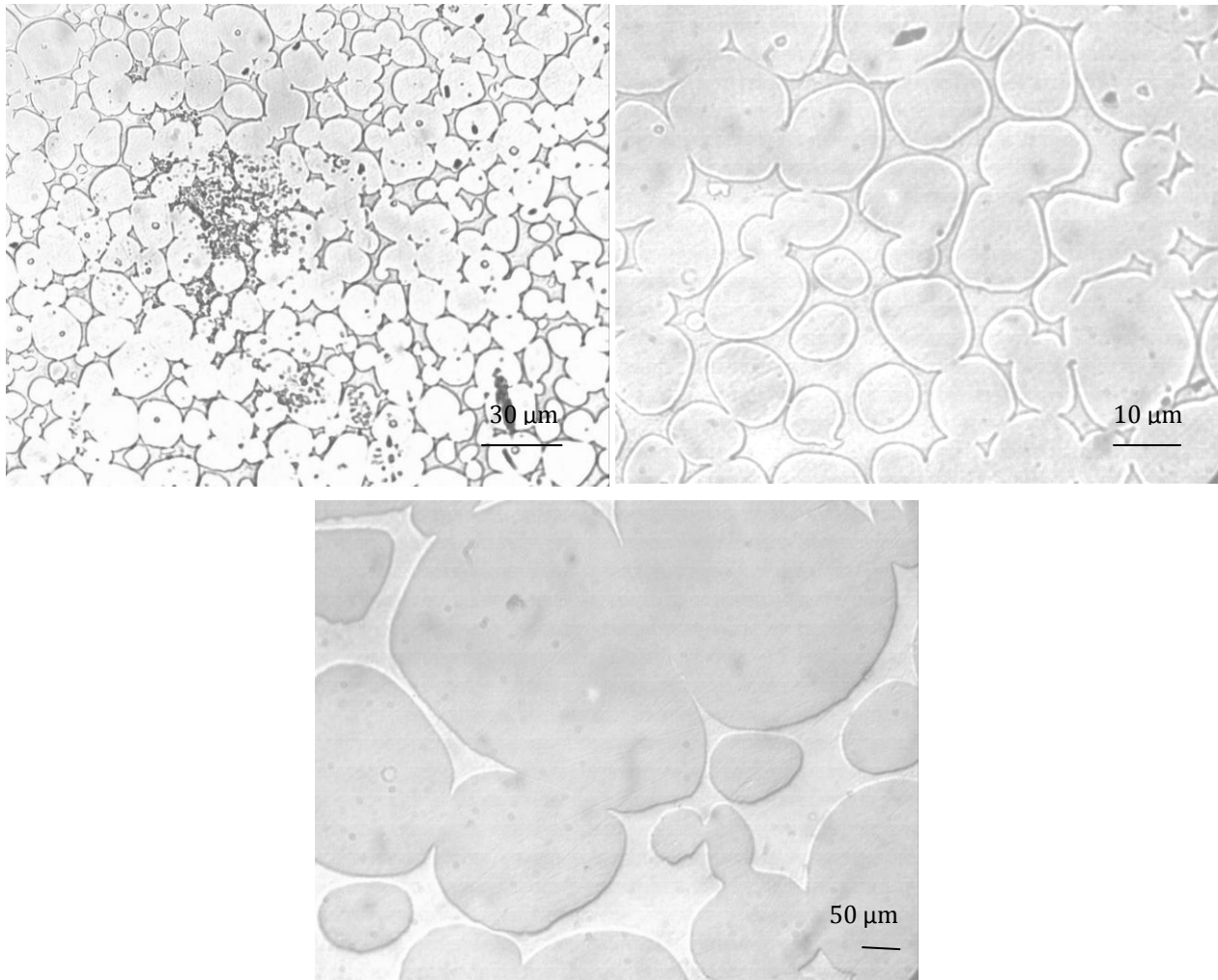


Figure 4.2.1: Metallographic photographs showing the W particles as well as the Ni-Fe matrix. Original magnifications: 20X, 50X, and 100X respectively. Etchant: Nital.

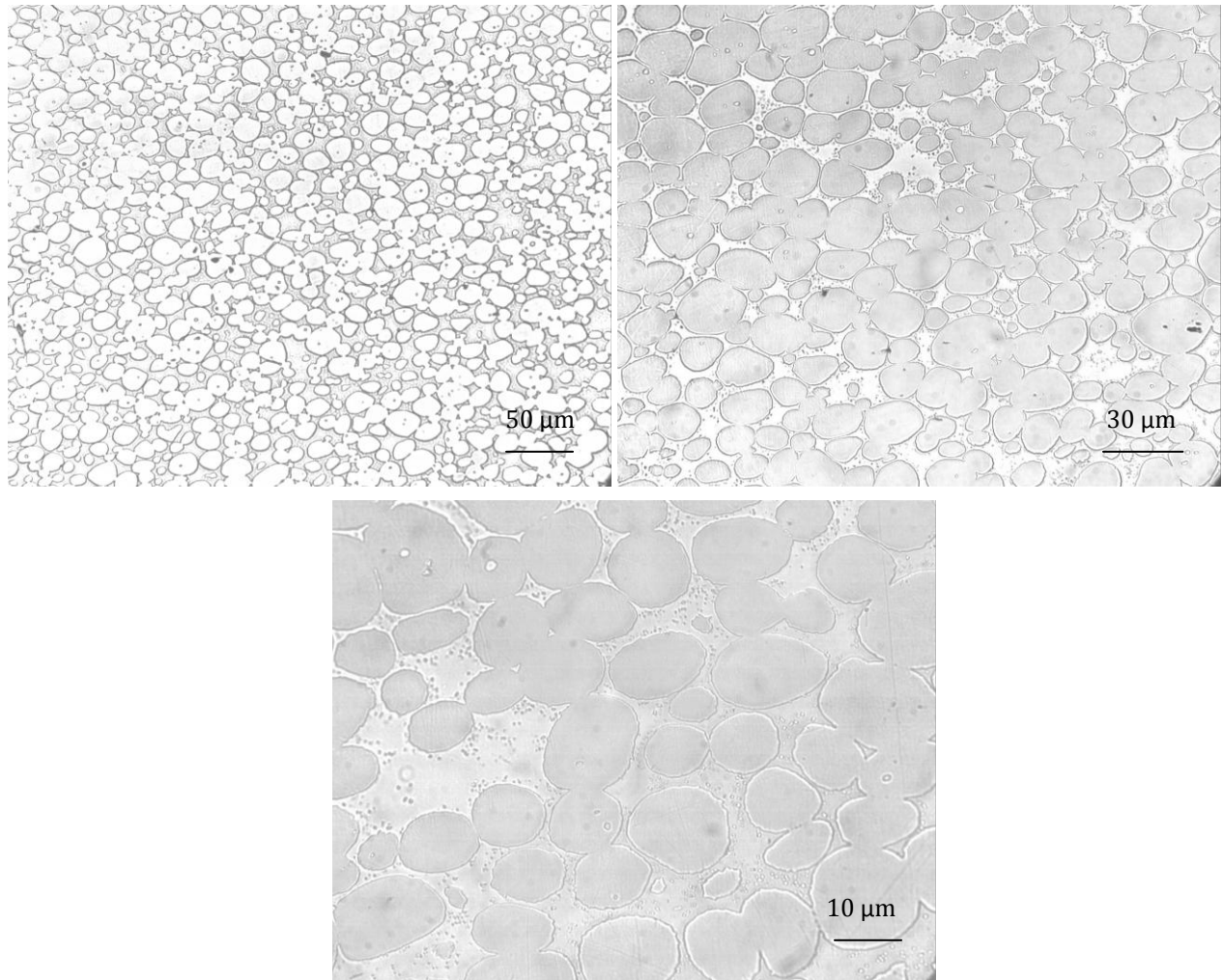


Figure 4.2.2: Representative microstructural features for W-Ni-Co alloy consisting of nearly spherical W particles. Original magnifications: 10X, 20X, and 50X respectively. Etchant: Nital.

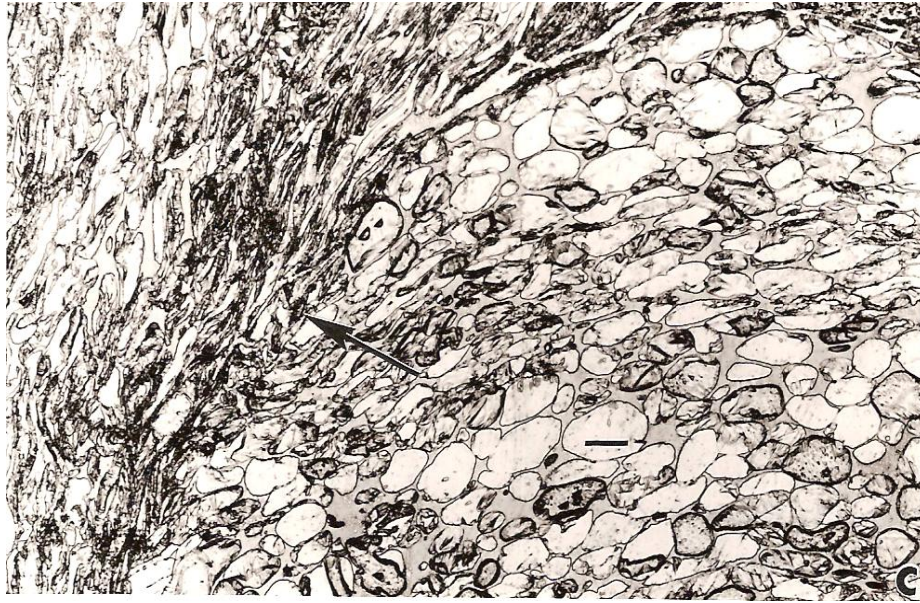


Figure 4.2.3: Microstructure illustrates the accommodation of a heavily deformed region in a WHA penetrator rod [22].

4.3 Particulate Characterization by SEM

Figure 4.3.1 shows a typical stage 6 or an approximate 2 μm cut point particulate from cascade impactor collectors observed directly in the SEM. The magnification on this figure is 5.0kx; it shows particle aggregates for a W-Ni-Fe projectile firing. The dominant element shown in the EDS spectrum is Fe, as expected from the particle analyses shown in Table 1. Some of the W is also observable, Ni is not detectable. It is not possible to separate the projectile matrix Fe from the mild steel Fe target contribution, which is not very significant. Figure 4.3.2 shows other particles ranging from 1 μm to 2 μm in the same stage at two different magnifications: 25kx and 50kx. Most of these particles are representative of Fe.

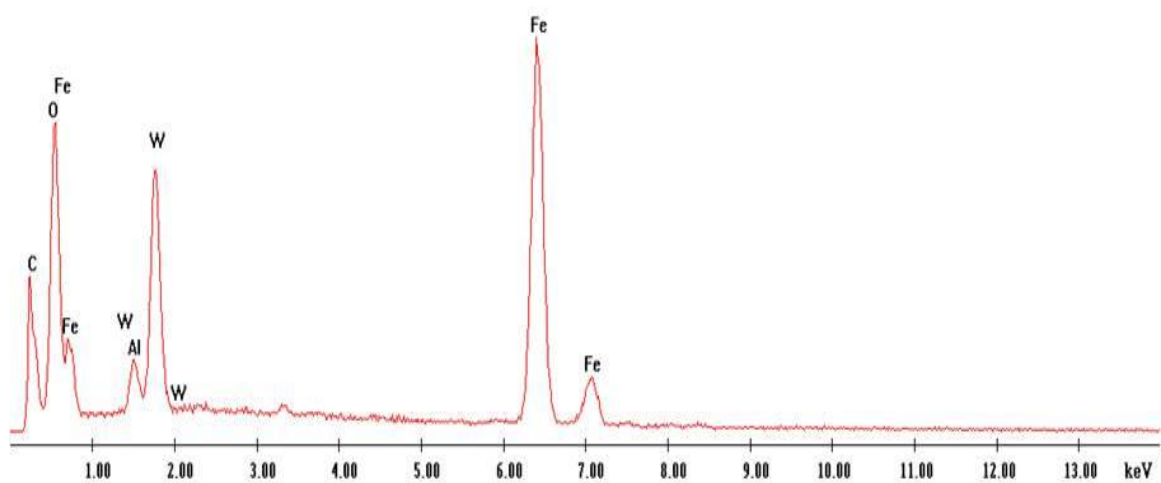
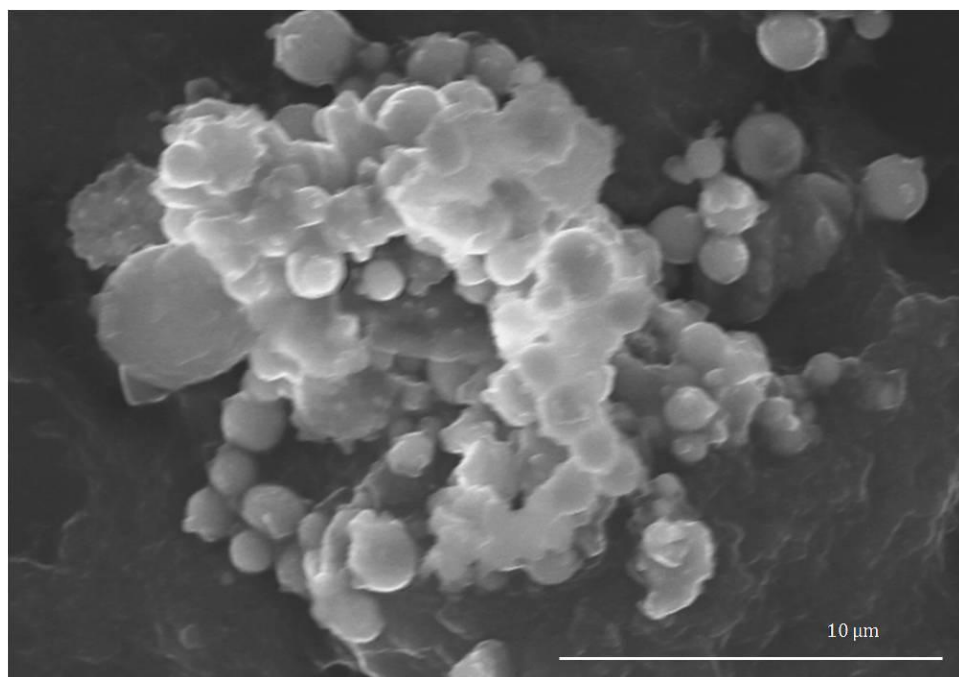


Figure 4.3.1: (Top) Image showing particulate aggregates from a W-Ni-Fe firing. Original magnification: 5.0kx. (Bottom) EDAX spectrum collected on the same area as image above.

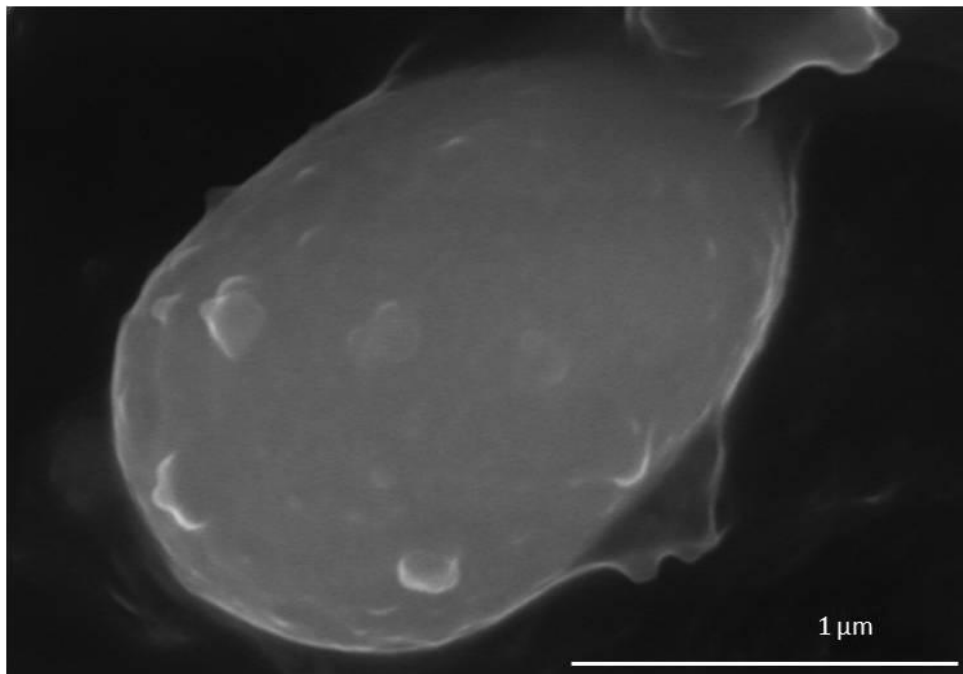
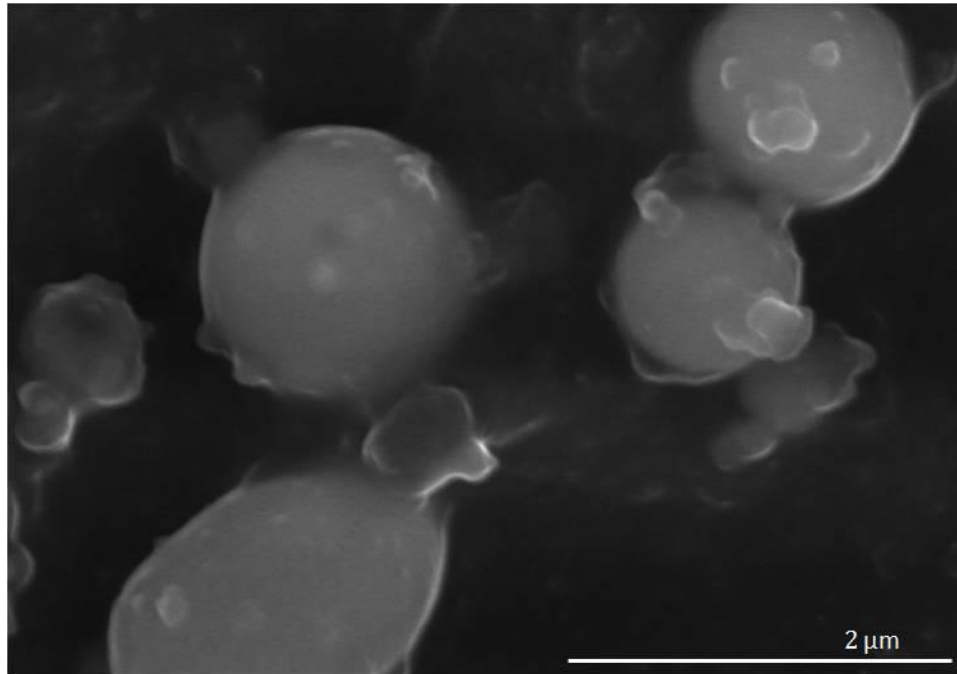


Figure 4.3.2: (Top) Shows particles in another region of stage 6 ranging from 1 μm to 2 μm . (Bottom) Higher magnification view of the particle on the bottom left of the above image. Original magnifications: 25.0kx and 50.0kx respectively.

Figure 4.3.3 illustrates particles similar to the particles in Figure 4.3.2 which are also from stage 6, but these particles correspond to Event 5 or the W-Ni-Co cascade impactor collections. The particles in this figure appear more agglomerated than the particles in Figure 4.3.2. Figure 4.3.4 shows another area on the same filter at 5.0kx. The EDS scale shows a propensity of target Fe, and there is no Ni or Co detected. The Al peak shown in this figure arises from an aluminum alloy windshield and tail fin assemblies which are noted in Figure 2.2.4. These windshield and tail fin assemblies are not always included in penetration collections [6].

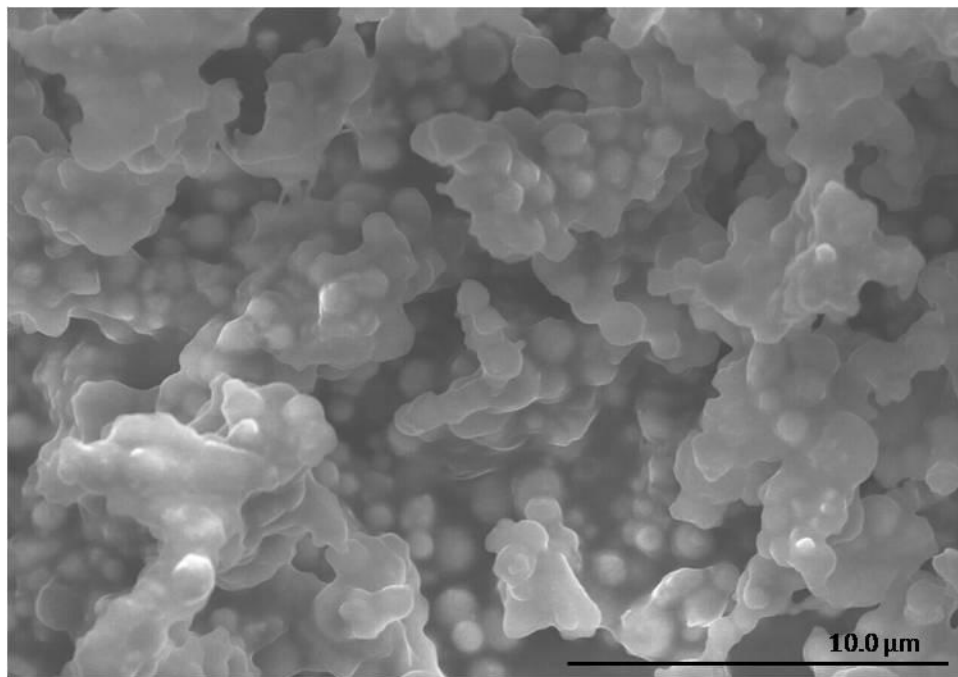


Figure 4.3.3: Illustrates particles that look more agglomerated than the particles in Figure 4.3.2. Original magnification: 5.0kx.

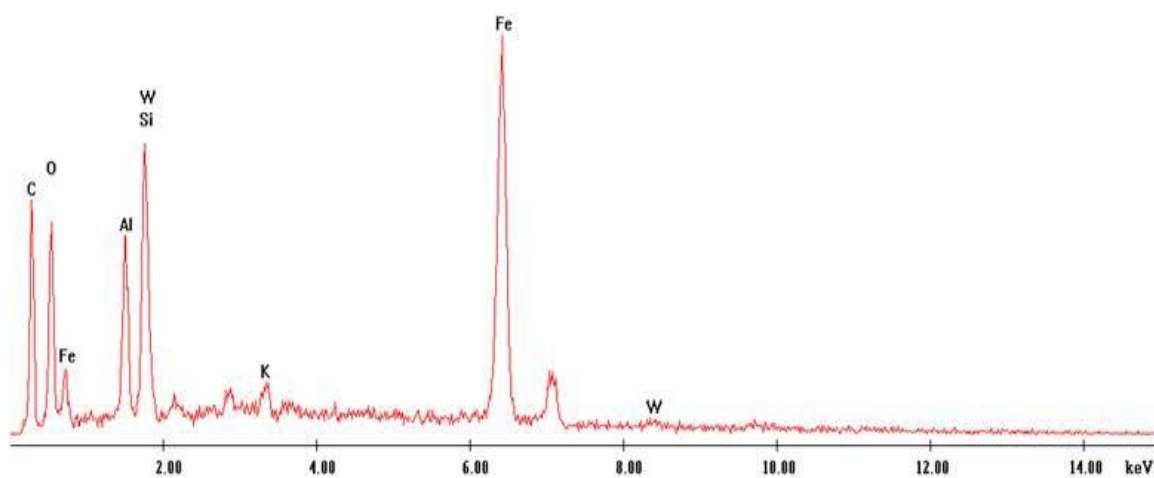
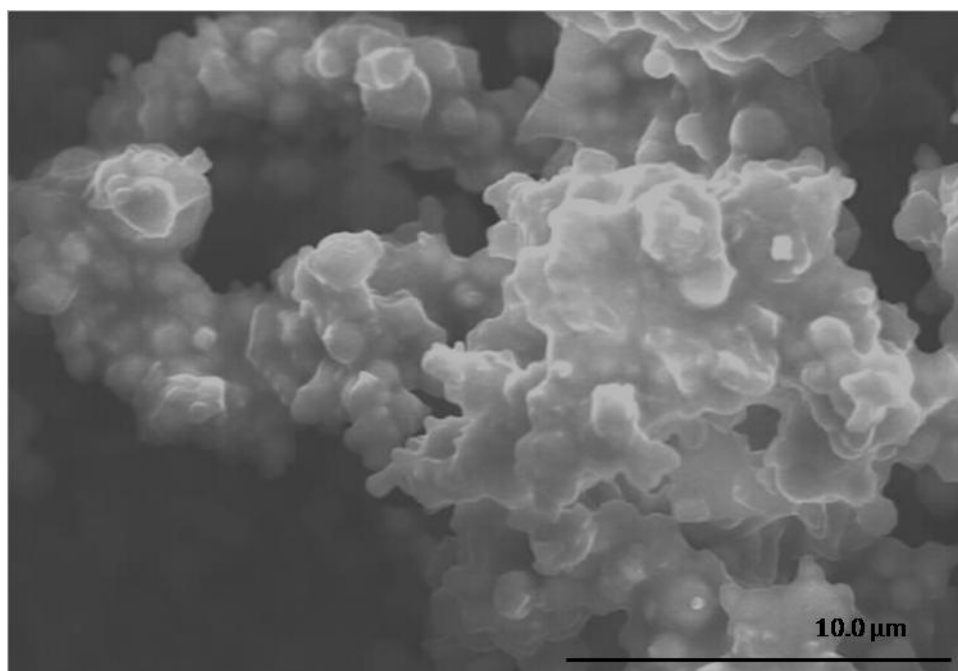


Figure 4.3.4: (Top) Shows an agglomerated region of particles similar to Figure 4.3.3 at the same magnification. (Bottom) EDS spectrum obtained for this area that revealed a high Al peak.

Figure 4.3.5 shows, by SEM, particles observed from the different MCE or single-filter collections for both W-Ni-Fe and W-Ni-Co projectile firings. These images were taken at 7.0kx and 15.0kx, respectively. As can be observed, following gold sputtering, the images still appear blurred without resolution. Since clear images were not obtained by observing the particles on the filter, the particles were scraped off and observed without the filter.

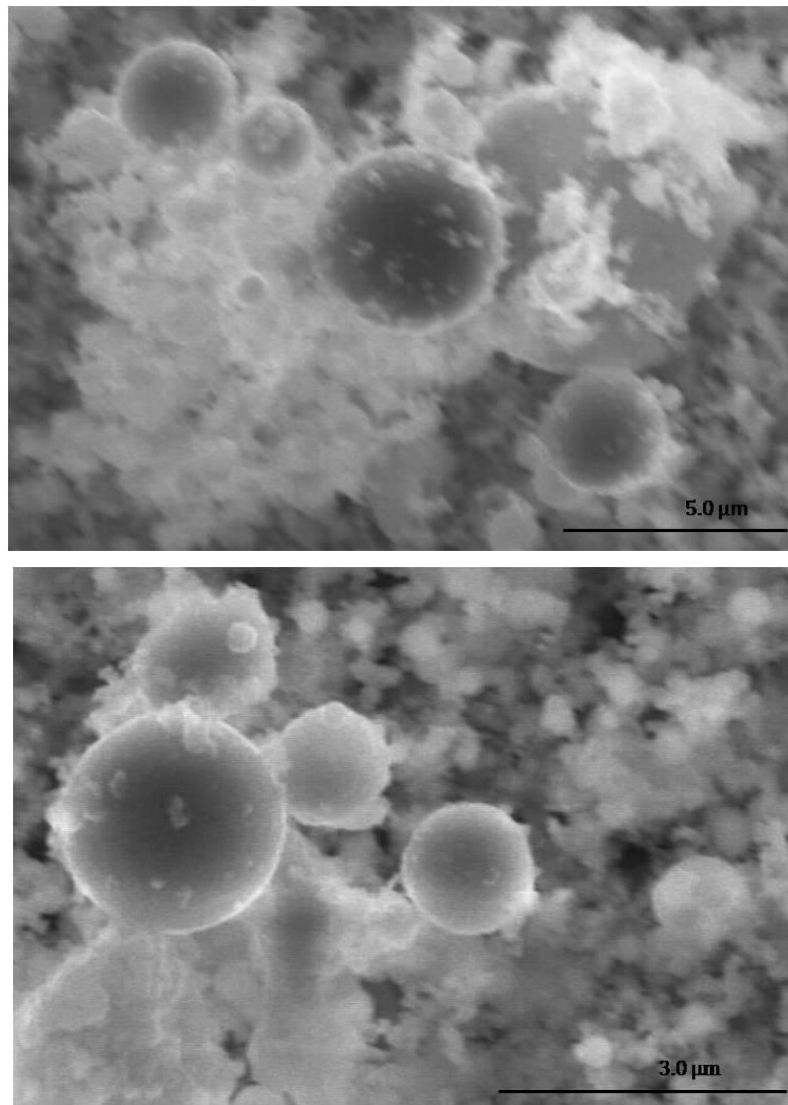


Figure 4.3.5: Both images show particles for both alloys on the filter at 7.0kx and 15.0kx.

Figure 4.3.6 shows an image from shot #3 for the W-Ni-Fe alloy at 40.0kx. This image illustrates noticeable clarity in contrast to the previous images in Figure 4.3.5. The image in Figure 4.3.6 and the following SEM images were observed without the filter and placed on an electrically conducting support which eliminated the majority of the charging in the specimens. The particles were easier to observe at higher magnifications. At 40.0kx the particulates in Figure 4.3.6 that are smaller than 0.5 μm are observable as pointed by the black arrows. The EDS results from Figure 4.3.6 show a significant oxygen peak that suggests that many of the particles may be oxides: Fe-O or Fe_2O_3 as suggested in a previous study by Gold [5] (see Figure 4.3.7). Figure 4.3.8 shows a higher magnification view of two particles from Figure 4.3.6 also demonstrating the spherical conformation.

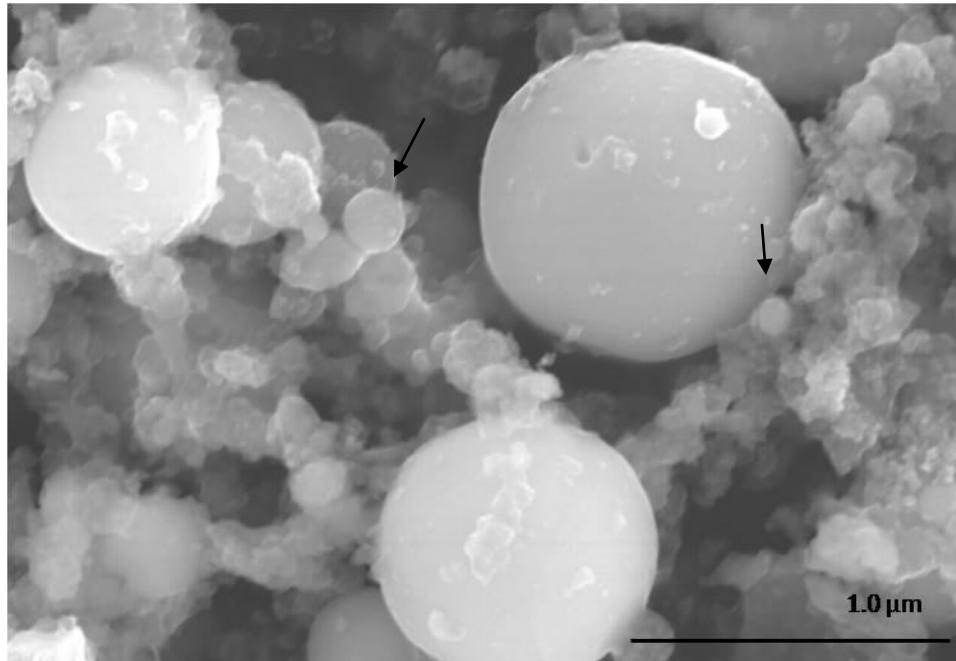


Figure 4.3.6: Illustrates particles smaller than 0.5 μm at an original magnification of 40kx.

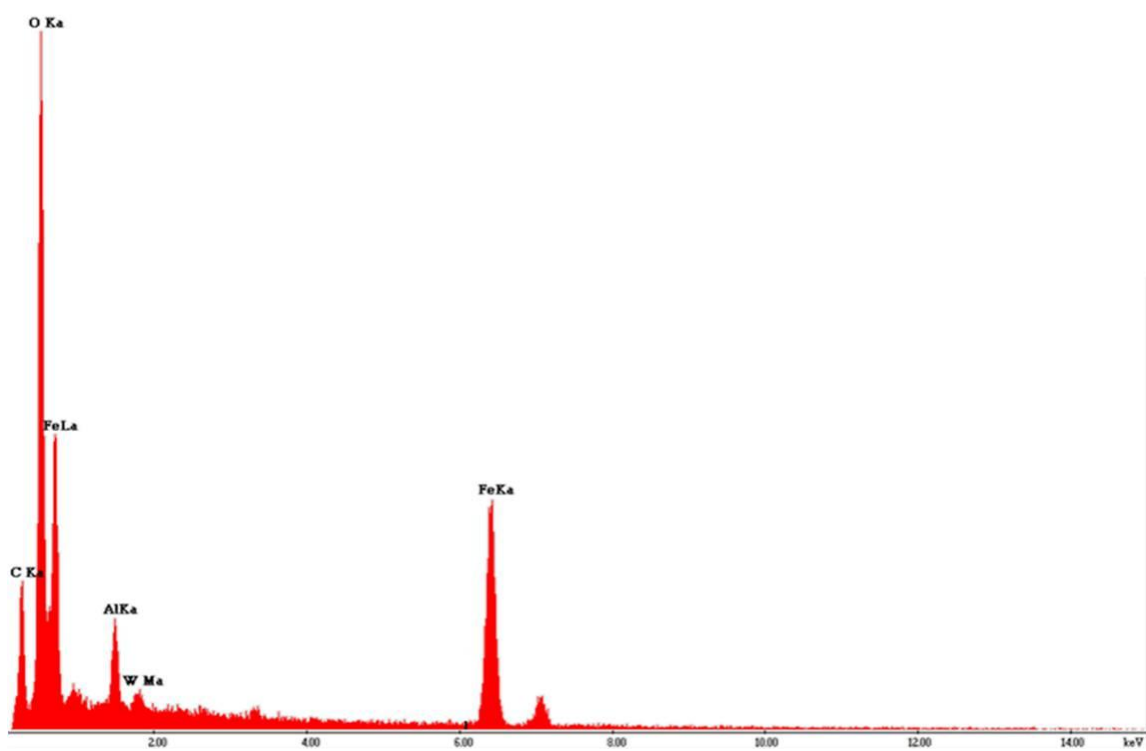


Figure 4.3.7: EDS spectrum for Figure 4.3.6 showing oxygen as the dominant peak, as well as some Fe, Al and W contents.

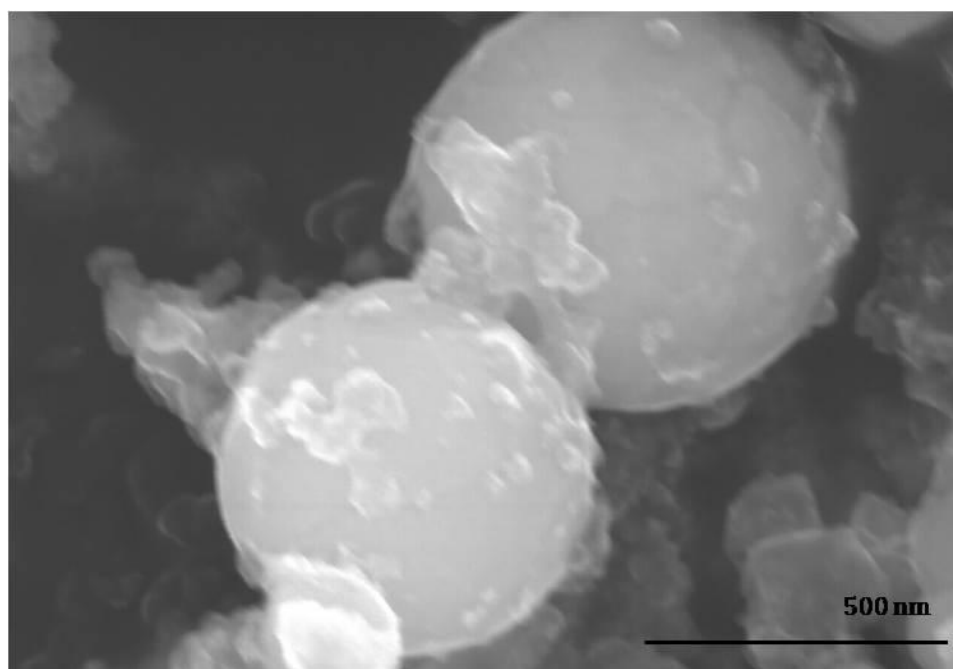


Figure 4.3.8: This image represents an area of two particles that range from 500 nm to 750nm. Original magnification: 80.0kx.

Figure 4.3.9 illustrates an SEM image from shot #10 also for the W-Ni-Fe single-filter collections. The EDS spectrum for this image shows a composition similar to the spectra for shot #3 (refer to Figure 4.3.10). This spectrum was obtained by doing a point analysis on the particles pointed by the black arrow that range from ≈ 0.1 to $0.2\ \mu\text{m}$. A small quantity of potassium is revealed in the spectrum that may be a remainder from the testing process or a combustion product. Figure 4.3.10 shows the quantification analysis for this spectrum in which Fe has the complete dominance of more than 40 weight percent of the total, with some W (≈ 11 Wt. %).

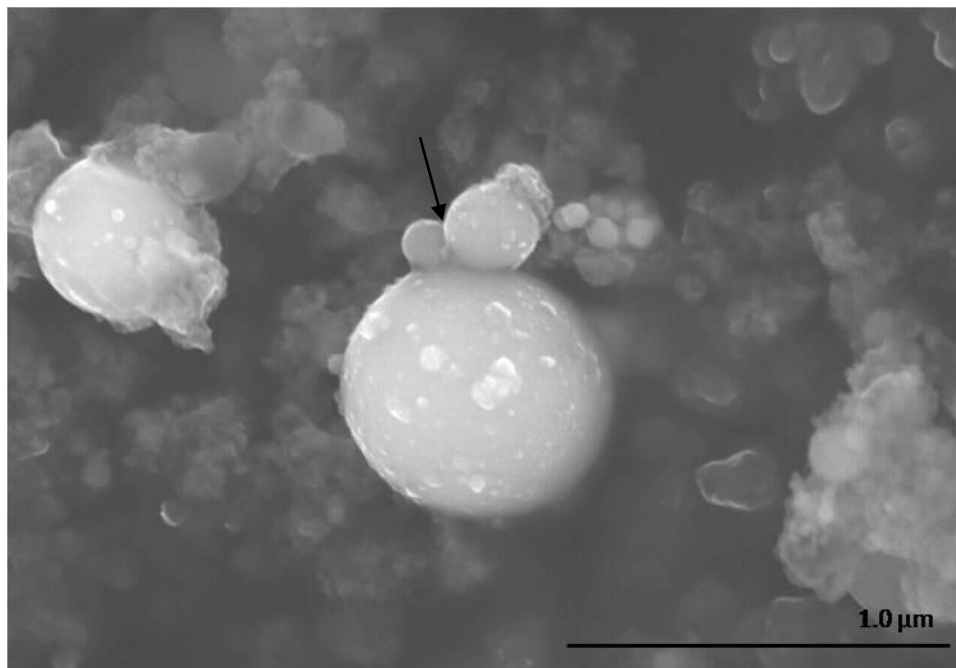
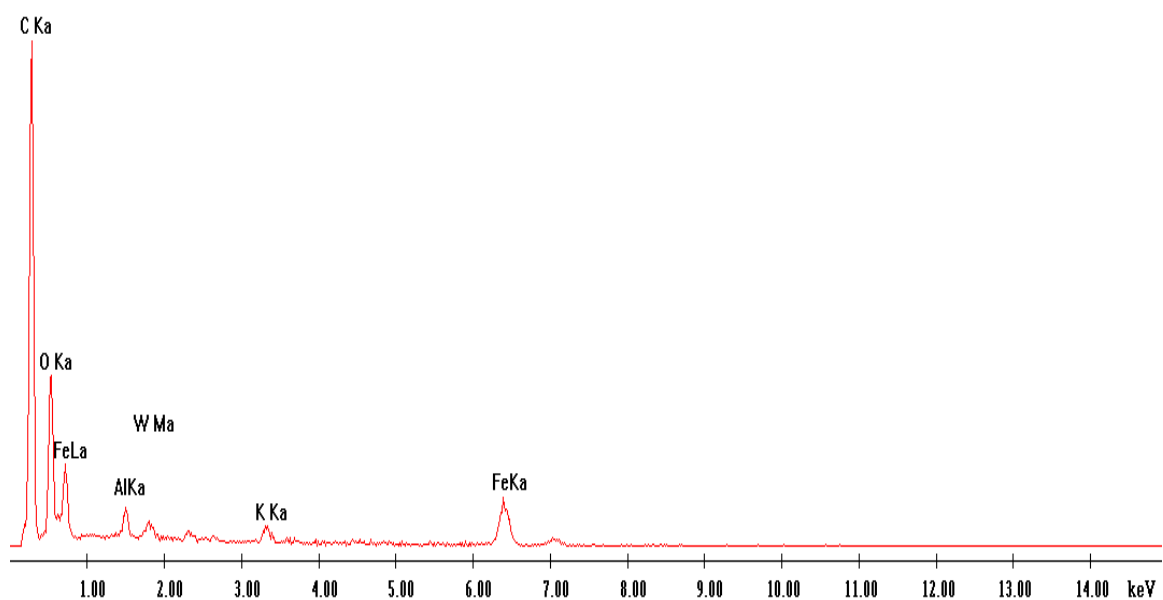


Figure 4.3.9: Image from shot #10 also for the W-Ni-Fe projectile firings showing particles approximate to $0.1\ \mu\text{m}$. Original magnification: 50.0kx.

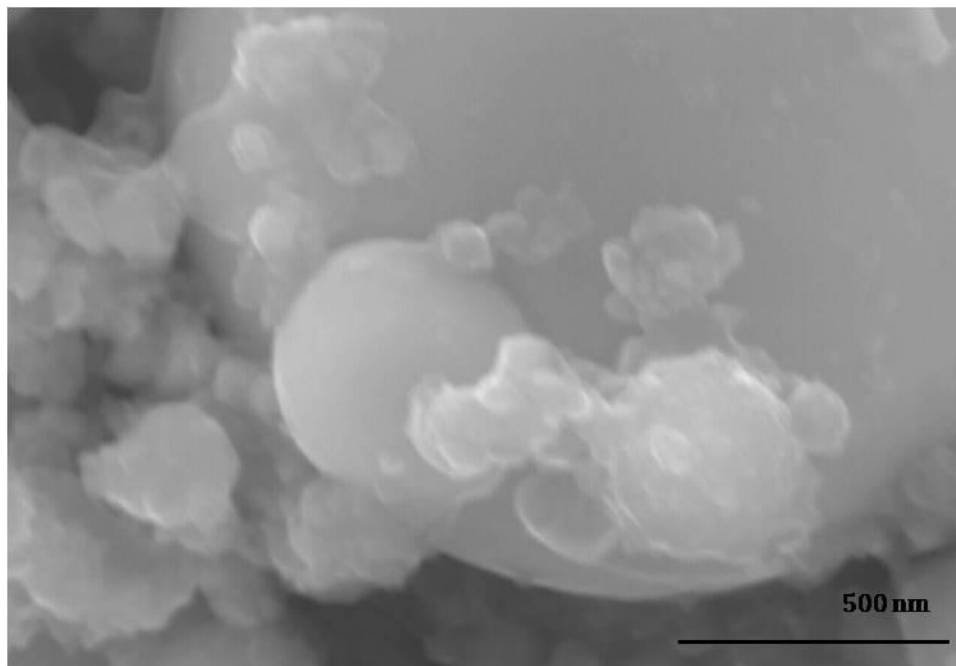


Elem	Wt %	At %	K-Ratio	Z	A	F
FeL	35.64	35.73	0.2878	1.0070	0.8017	1.0001
AlK	5.64	11.69	0.0297	1.1139	0.4735	1.0005
W M	11.23	3.42	0.0682	0.7807	0.7778	1.0000
K K	3.60	5.15	0.0350	1.0832	0.8865	1.0131
FeK	43.90	44.01	0.4423	1.0126	0.9910	1.0041
Total	100.00	100.00				

Element	Net Inte.	Backgrd	Inte. Error	P/B
FeL	22.80	1.92	3.20	11.87
AlK	12.15	3.82	5.18	3.18
W M	7.52	3.42	7.13	2.20
K K	7.82	2.42	6.43	3.23
FeK	31.12	0.60	2.58	51.87

Figure 4.3.10: (Top) EDS spectrum from a point analysis showing a small potassium peak. (Bottom) The quantification results for the EDS spectrum shows dominance of the Fe over all the percentage.

Figure 4.3.11 represents SEM images from shots #11 and #13, respectively. These shots are representative of W-Ni-Co single-stage collector filters. Figure 4.3.11 shows two images taken at 70.0kx and 50.0kx respectively. These SEM views are essentially the same or similar to other projectile firing events and filter collections shown in the previous figures for W-Ni-Fe. The EDS for these images are also similar to previous spectra with some variations in W concentrations (refer to Figure 4.3.12). Ni nor Co concentrations were detected in these EDS spectra and that is true for all spectra recorded under different magnifications for the different compositions. The W-Ni-Co single collector also shows some K that may represent combustion products from the projectile firing as previously mentioned.



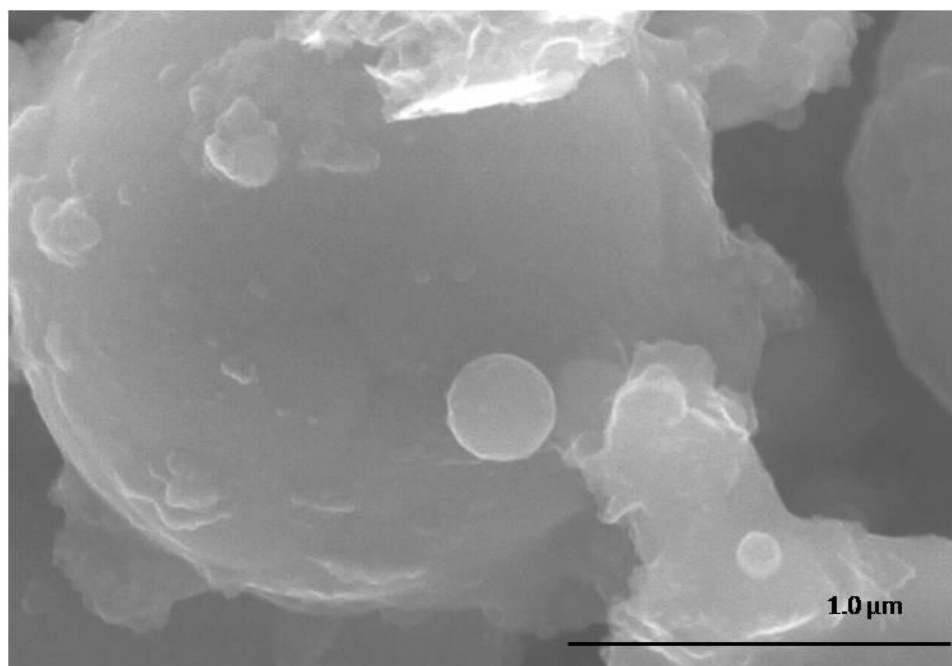
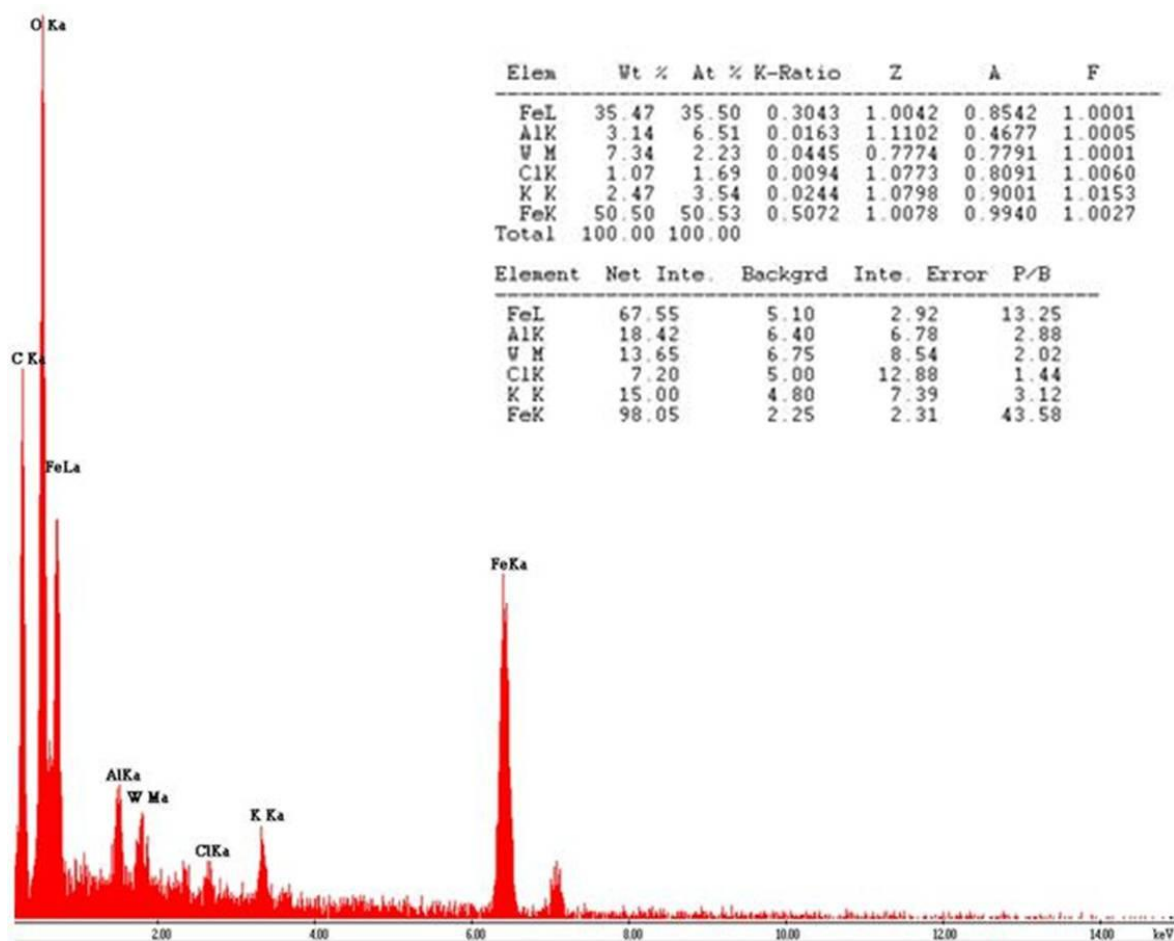


Figure 4.3.11: (Top)SEM image of a small area in shot #11. (Bottom)Shot #13 image shows a large individual particle. Original magnifications: 70.0kx and 50.0kx respectively.



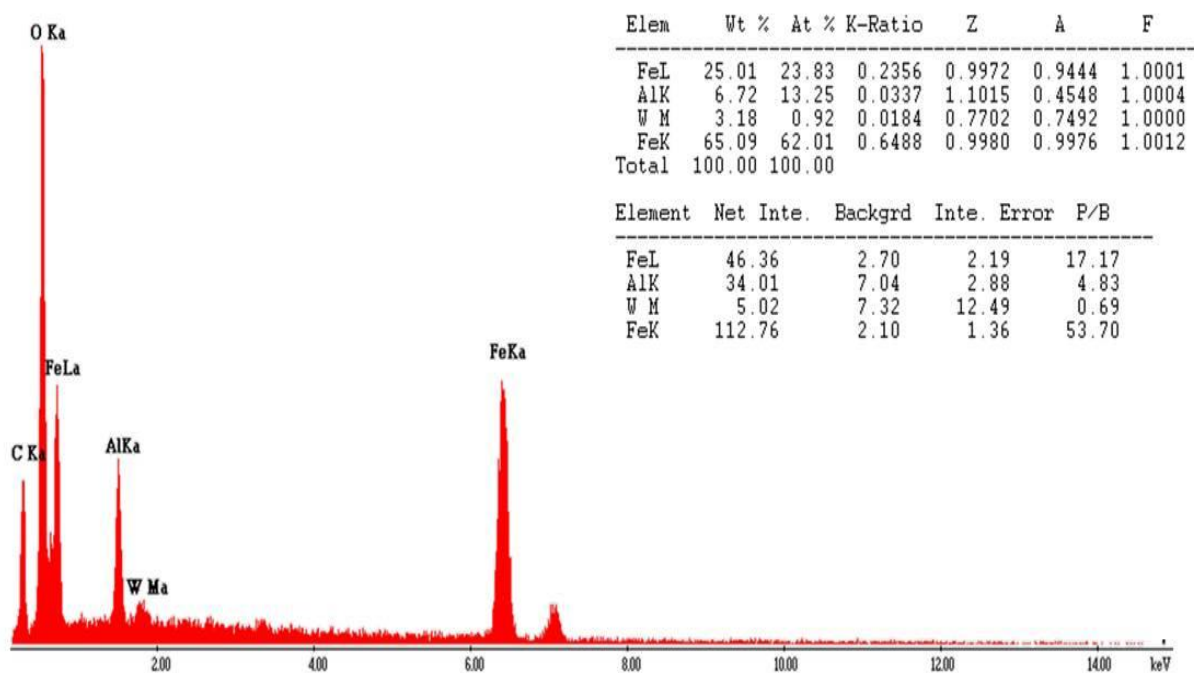


Figure 4.3.12: (Top) EDS spectrum for shot #11 with its respective quantification results.
(Bottom) EDS spectrum for shot #13 showing Fe as the major weight percent.

The W-projectile matrix including either the Ni-Fe or the Ni-Co matrix represents about 7 weight percent of the projectile or roughly 3 to 4 weight percent for each element which represents less than 0.01 weight percent for the total aerosol collection. This calculation is taking into consideration that the 10 steel target plates are perforated, the diameter of the penetration hole is ≈ 0.8 cm, and the total projectile erosion is approximately 80 percent. As a result, this contribution would not be detected in the SEM/EDS analysis because it is well below the nominal elemental sensitivity of ≈ 0.5 to 1.0 percent. It might be concluded that since neither the W nor the alloy matrix particles have been observed significantly in these analyses (SEM/EDS), the W alloy particulates are

mainly in the $>10\ \mu\text{m}$ size range, which would not allow for their collection; although DRX erosion products as implicit in Figure 4.2.3 below $\approx 2\ \mu\text{m}$ would be collected.

4.4 Particulate Characterization by TEM

The following figures show an analytical sequence for TEM observations of small aggregates of particulates at two magnifications ranging from 53.8kx to 84.3kx. These particulates were scrapped from a single-stage filter collector (shot#3) for W-Ni-Fe. Figure 4.4.1.a shows a bright-field image of the aggregate at 54.4kx. Figure 4.4.1b shows the SAED pattern where only a few diffraction spots are observable. Figure 4.4.1c shows the dark-field image of Figure 4.4.1a utilizing the specific diffracting spot pointed by the white arrow in Figure 4.4.1b. In the dark-field image the crystallinity of the material is observed.

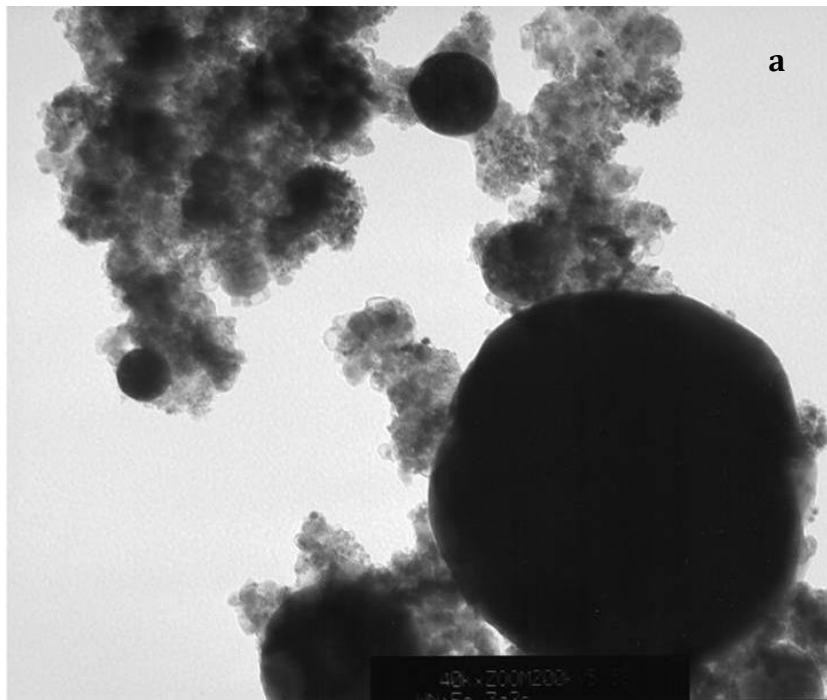


Figure 4.4.1a: Bright-field image of the aggregate at an original magnification of 53.8kx.

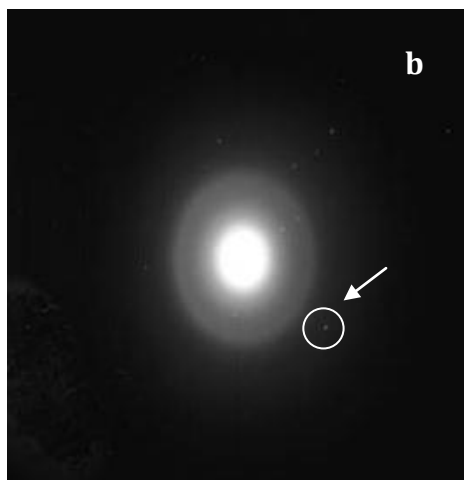


Figure 4.4.1b: Image shows the selected-area electron diffraction pattern.

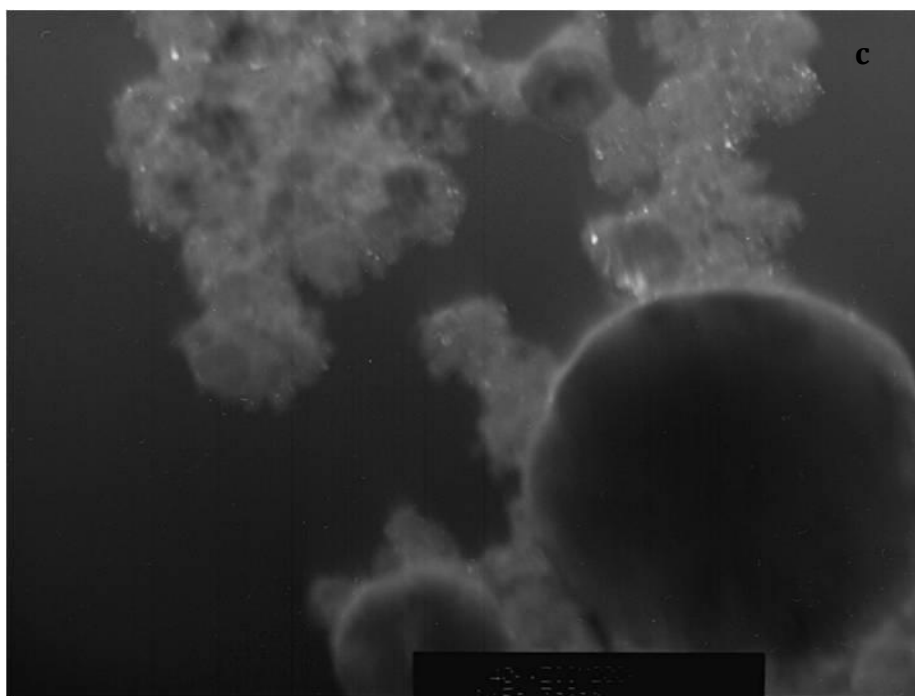


Figure 4.4.1c: Dark-field image on the same area as Figure 4.4.1a.

Figure 4.4.2 shows another image from the same shot at a higher magnification. This figure shows smaller crystal fragments that are indicated by the arrows. Figure 4.4.2 also shows the corresponding diffraction pattern for this area.

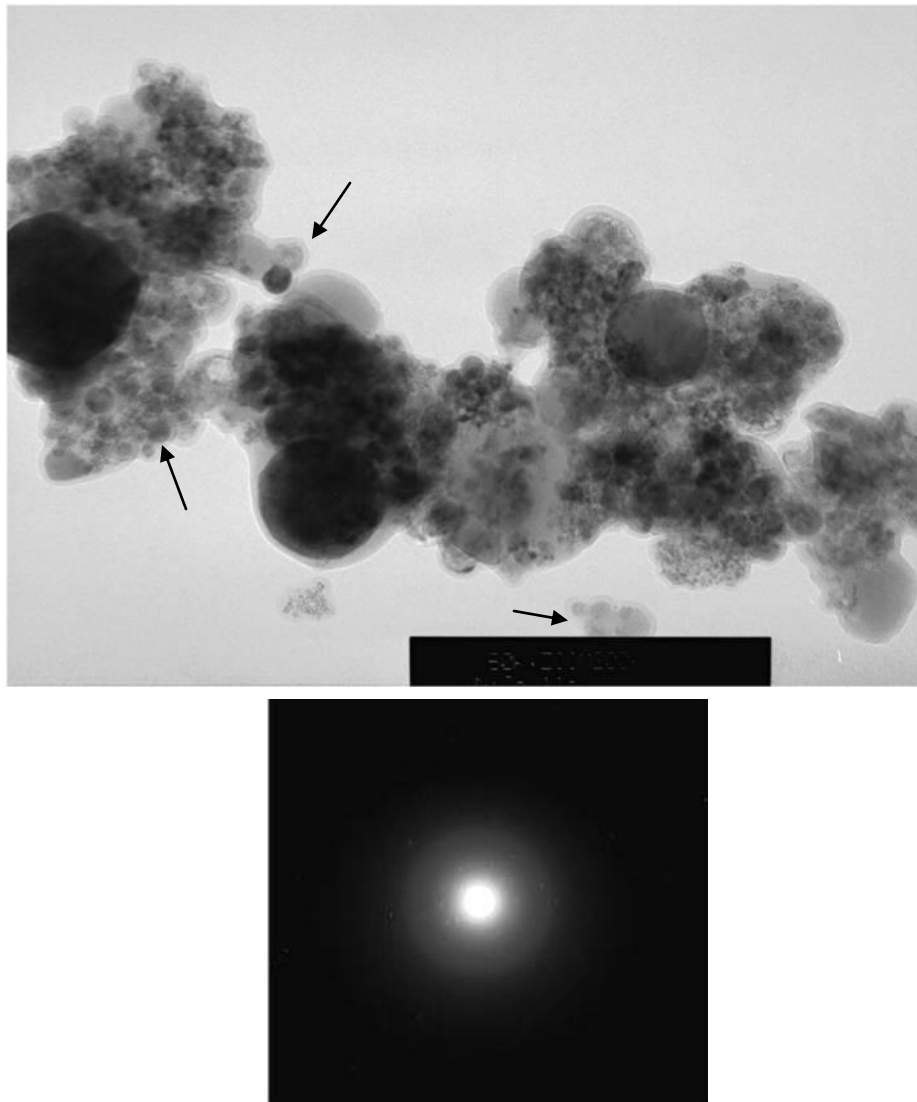


Figure 4.4.2: (Top) Area showing different sizes of particles. Original magnification: 84.3kx. (Bottom) This image shows the diffraction pattern showing only a few spots.

Figure 4.4.3 shows TEM images in bright and dark-field containing small nanoparticulates that range from ≈ 10 to 50 nm. These images are representative of the W-Ni-Co (shot #11) projectile firings in the single-stage collector filters. Figure 4.4.3a shows the bright-field image at 54.4kx. Figure 4.4.3b shows the SAED pattern with prominent arrangement of diffraction spots from various crystalline particles. A number of nanoparticulate aggregates are also visible in the dark-field image (refer to Figure 4.4.3c). In fact, Figure 4.4.3c illustrates different crystalline particles with diameters less than 10 nm to 1.1 μm .

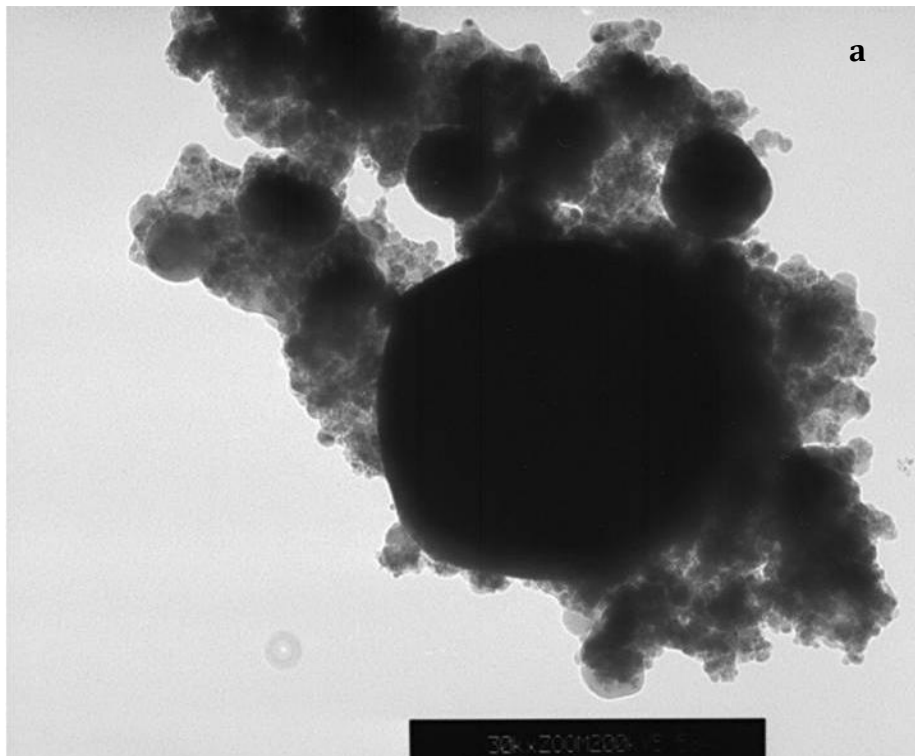


Figure 4.4.3a: Particle aggregate for W-Ni-Co projectile firing. Original magnification: 54.4kx.

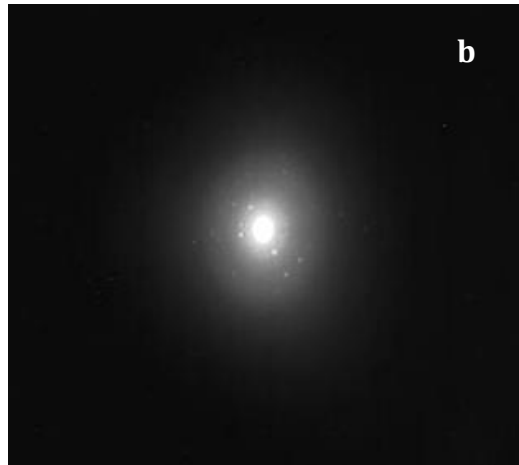


Figure 4.4.3b: SAED pattern showing different spots from the different crystalline particles.

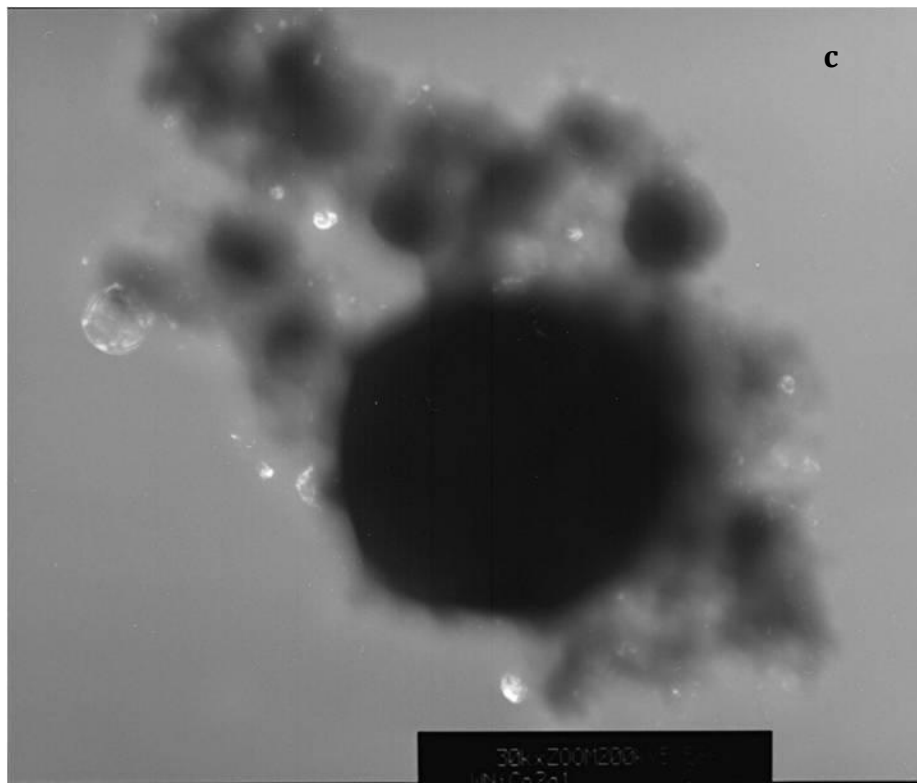


Figure 4.4.3c: Image represents dark-field of the image in Figure 4.4.3a. Original magnification: 54.4kx.

Figures 4.4.4 (Event 3) and 4.4.5 (Event 5) provide additional TEM images for comparison of the cascade impactor collector filters. Both figures show bright-field images for the W-Ni-Co projectile firings. Figure 4.4.4 shows two large aerosol particulates as well as smaller ones attached to them, pointed to by the black arrows. The SAED pattern shows a range of diffraction spots from this particulate area. Figure 4.4.5 also shows a bright-field image at 21.1kx with a wide distribution of particulates.

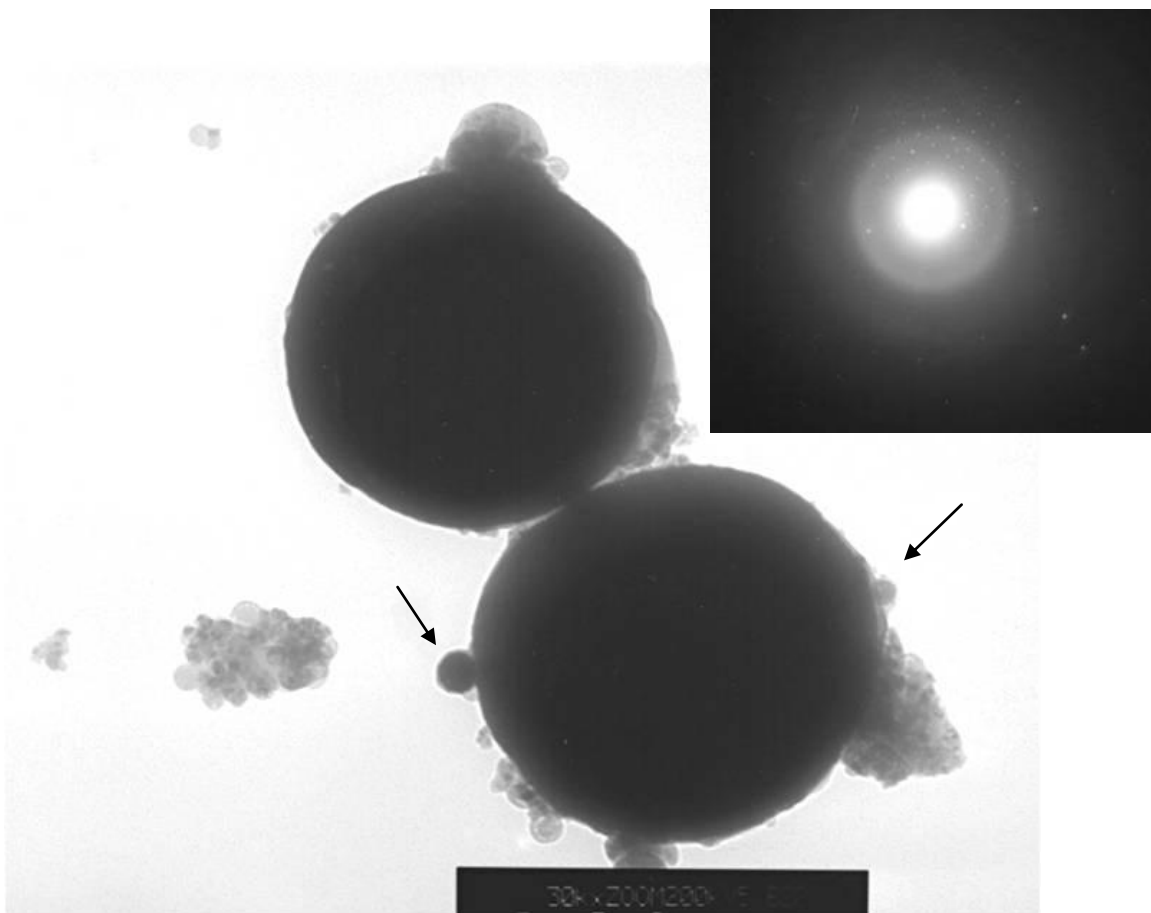


Figure 4.4.4: Bright-field image of different size aerosol particulates with its respective SAED pattern. Original magnification: 42.4kx.

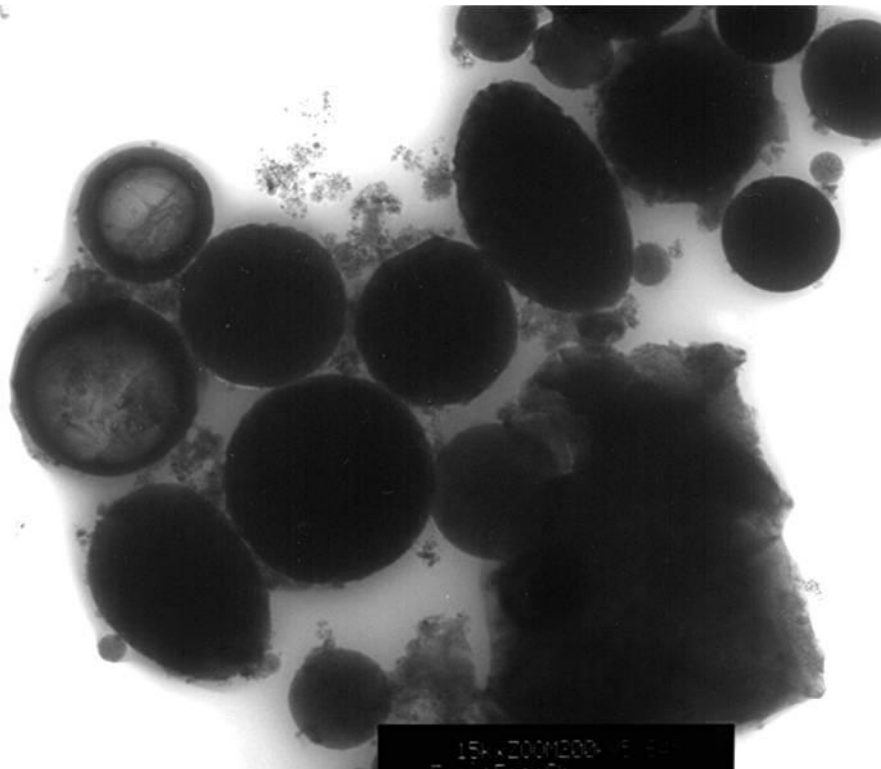


Figure 4.4.5: Bright-field image of wide distribution of crystalline aerosol particulates at a lower magnification than Figure 4.4.4.

The following figures show a sequence of high resolution TEM micrographs of small aggregate particulates scrapped from MCE filter for both W-Ni-Fe and W-Ni-Co. Figure 4.4.6a illustrates a bright-field image of the aggregate while Figure 4.4.6b shows the corresponding SAED pattern. Diffraction spots are not well observed because of the diffuse background; the arrow indicates a specific diffraction spot. Figure 4.4.6c illustrates the corresponding dark-field image of Figure 4.4.6a utilizing the diffraction spot at the arrow in Figure 4.4.6b. It can be noted that this particle is a bi-crystal with some microstructure visible on the left side (bright) of the crystal. Smaller (nano) crystals are also observed (refer to Figure 4.4.6c) that are ≈ 5 nm.

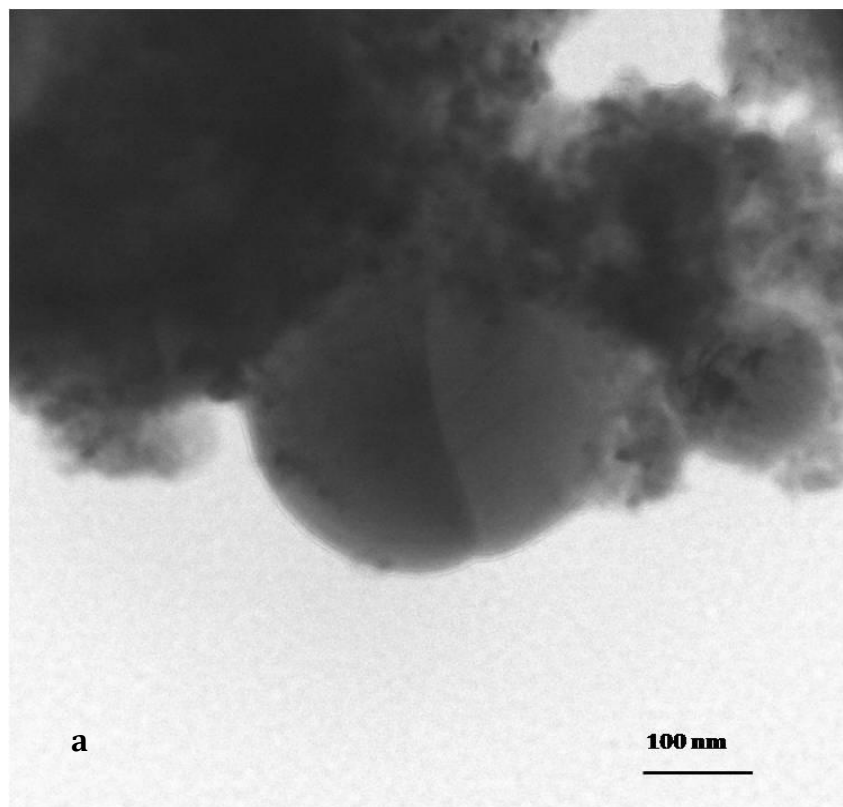


Figure 4.4.6a: Bright-field image of particulate aggregates. Original magnification: 30.0kx.

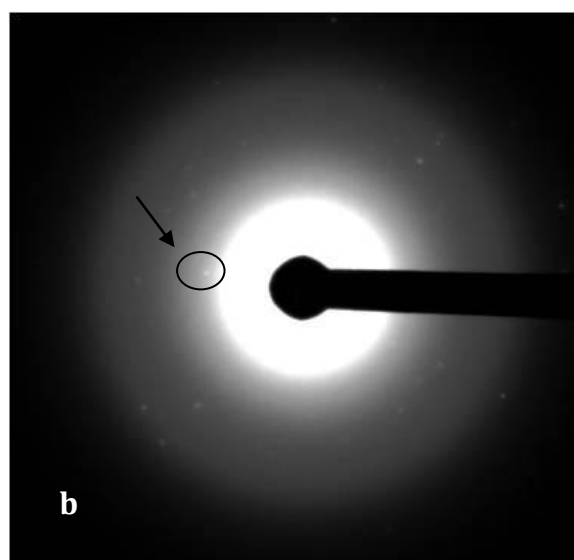


Figure 4.4.6b: SAED pattern with a diffuse background.

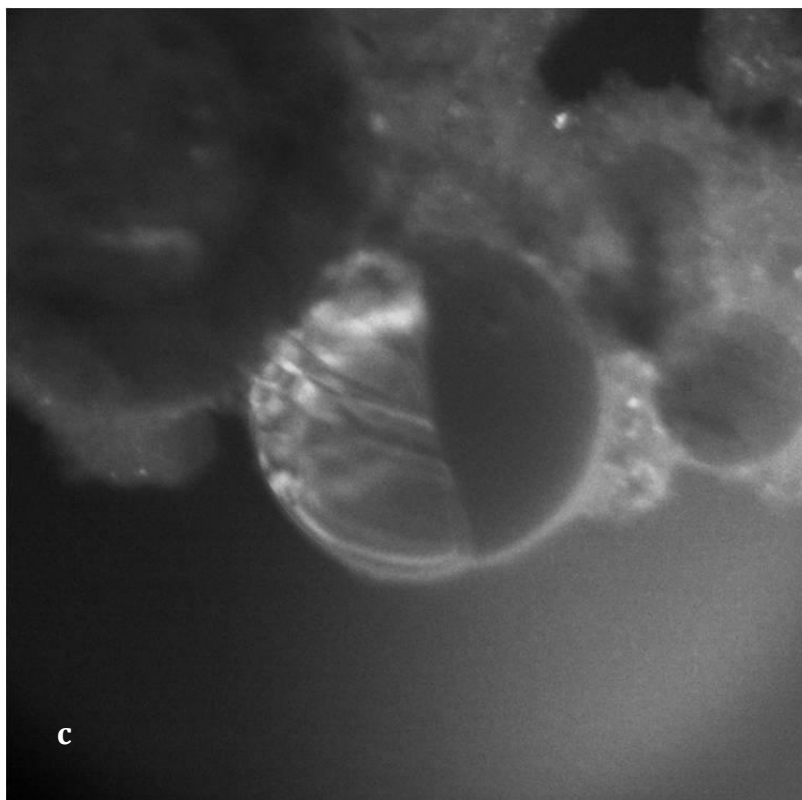


Figure 4.4.6c: Dark-field image using the diffraction spot in Figure 4.4.6b. Original magnification: 30.0kx.

All of the SAED patterns from Figures 4.4.1 to 4.4.6b show prominent arrays of diffraction spots from various crystalline particles, but there is also some diffuse diffraction, which is less prominent in the SAED pattern in Figure 4.4.6b. After careful examination of the bright-field images in these figures along with their respective SAED patterns suggests that some organic or carbon component of the aggregates is present. This is also reflected in the carbon peaks in all of the EDS results (refer to Section 4.3 (SEM/EDS)). Some of this organic debris represents residual combustion material as the rod projectiles were fired by a gun. Figures 4.4.7 and 4.4.8 confirm the presence of carbon component of the aggregates. Figure 4.4.7 shows an image taken at 20.0kx. Figure 4.4.8 illustrates the same area shown in Figure 4.4.7 but this figure was taken approximately one

or two minutes afterwards. It is possible to observe in Figure 4.4.8 the growth of dendritic structures that appear to be carbon nanotubes. These samples are directly exposed to high beam intensities, which causes rapid charging of the area, therefore growing these carbon nanotubes. L. E. Murr [34] has shown that samples that normally exhibit extremely rapid vibration at high beam intensities or image alterations at the edges of crystals are indicative of substantial and rapid charging of the area.

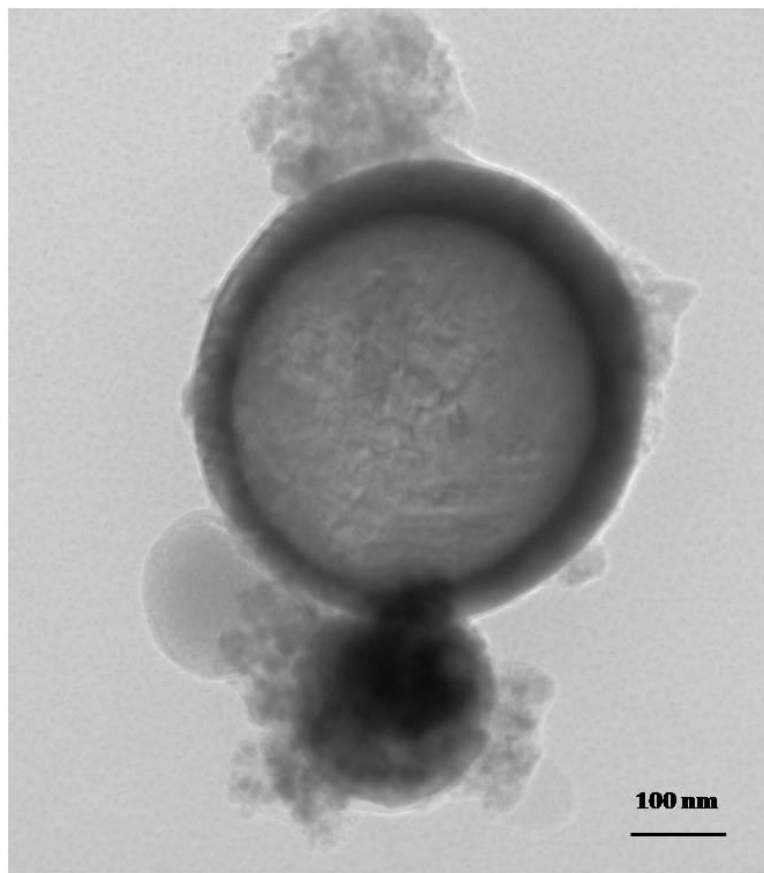


Figure 4.4.7: Image in bright-field showing a black halo around the big particle. Original magnification: 20.0kx.

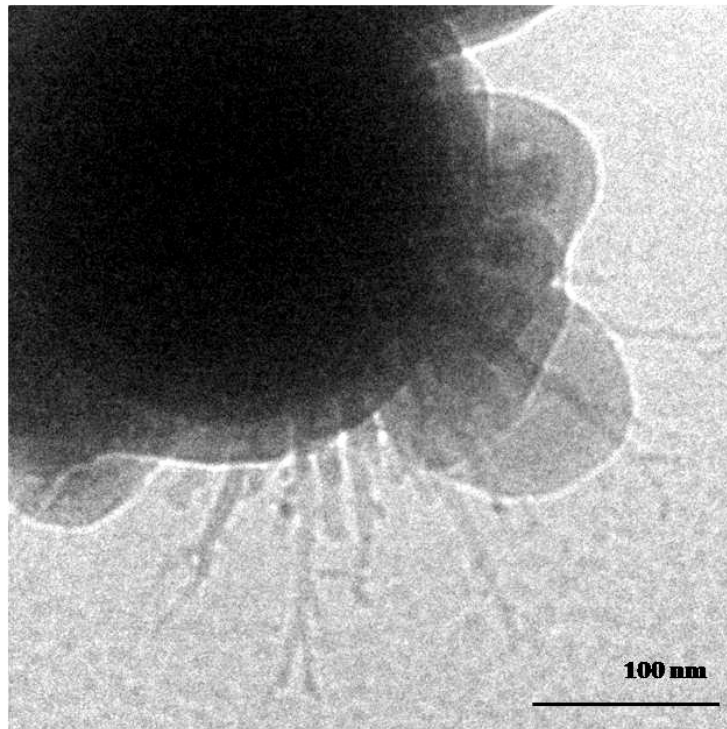
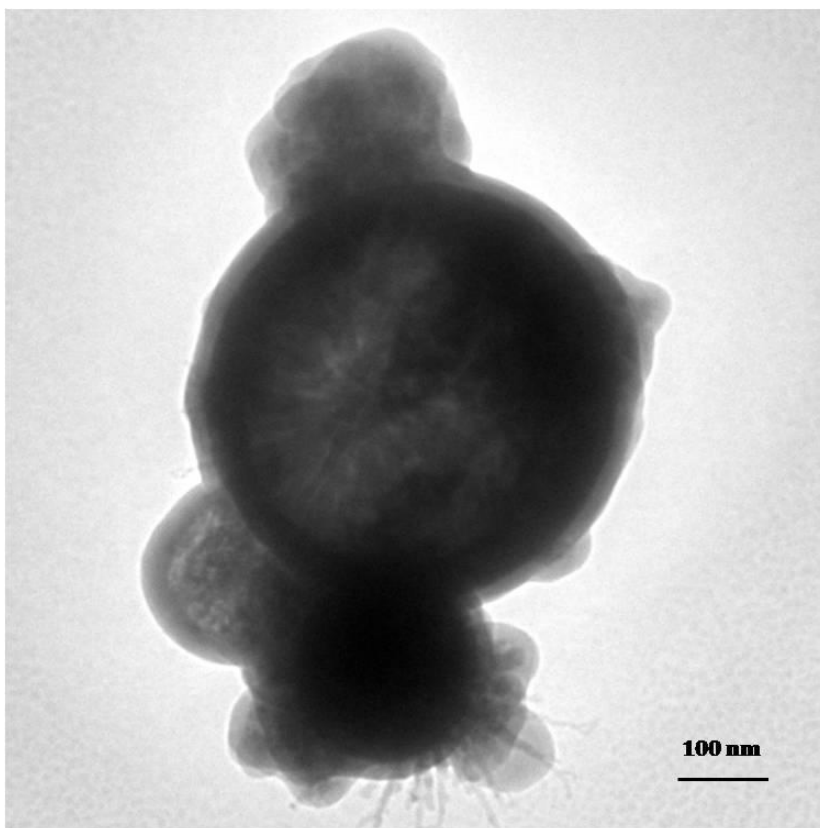


Figure 4.4.8: (Top) Image representing the same area as Figure 4.4.7 after beam charging. (Bottom) Image shows a higher magnification view of the dendritic structure. Original magnifications: 30.0kx and 40.0kx.

Pizaña et al. [19] have shown that for single-crystal W rods that penetrate RHA targets, there is a turbulent mixing zone between the W rod RET and the TET (refer to Figure 2.1.1). This zone is characterized by mechanical mixing and thermodynamic alloying due to localized melt, as a result, W DRX particles, dendritic Fe and W particles, and Fe_xW eutectic particles are produced. This turbulent mixing zone is a contributor to the debris field and aerosol particulates. The aerosol content for particulates $\leq 2 \mu\text{m}$ could include Fe target erosion particles, fine or ultra-fine W particles, and Fe_xW eutectic particles. The Ni content in the matrix could form a small fraction of Ni-Fe alloy [19]. The thermodynamic interaction of the projectile and target is complicated by the high-pressure in the system and the variation in melt compositions and actual melt phenomena associated especially with the nanoparticles.

As previously discussed (refer to Section 4.3) there is no detectable Ni or Co. However, specific areas of some of the nanoparticles or nanoparticle aggregates could represent the rod matrix or the matrix components. Figures 4.4.9 and 4.4.10 represent aggregated zones, including very small particles. Figure 4.4.9 shows a TEM image for a W-Ni-Fe particulate aggregate. The corresponding EDS spectrum reveals a Ni peak (refer to Figure 4.4.9b). The Cu peaks occur from the Cu TEM grid which helps to provide an internal calibration. The large particles as already stated represent Fe particles. Figure 4.4.10a represents a rod penetration collection for the W-Ni-Co alloy. This figure shows a large particle surrounded by C which appears to maintain the aggregate of nanoparticles together. As shown previously, this is a result from the large contribution of combustion products. Figure 4.4.10b shows the resultant EDS spectrum for the particle in Figure 4.4.10a. In the spectrum there is considerable Co but no detectable Ni as observed in

Figure 4.4.9b. These EDS results for both projectile firings are exemplars of the heterogeneous distribution on the aerosolized particulates. The grid is coated with formvar/SiO and this will also contribute into the EDS spectra results (refer to Figure 4.4.10b).

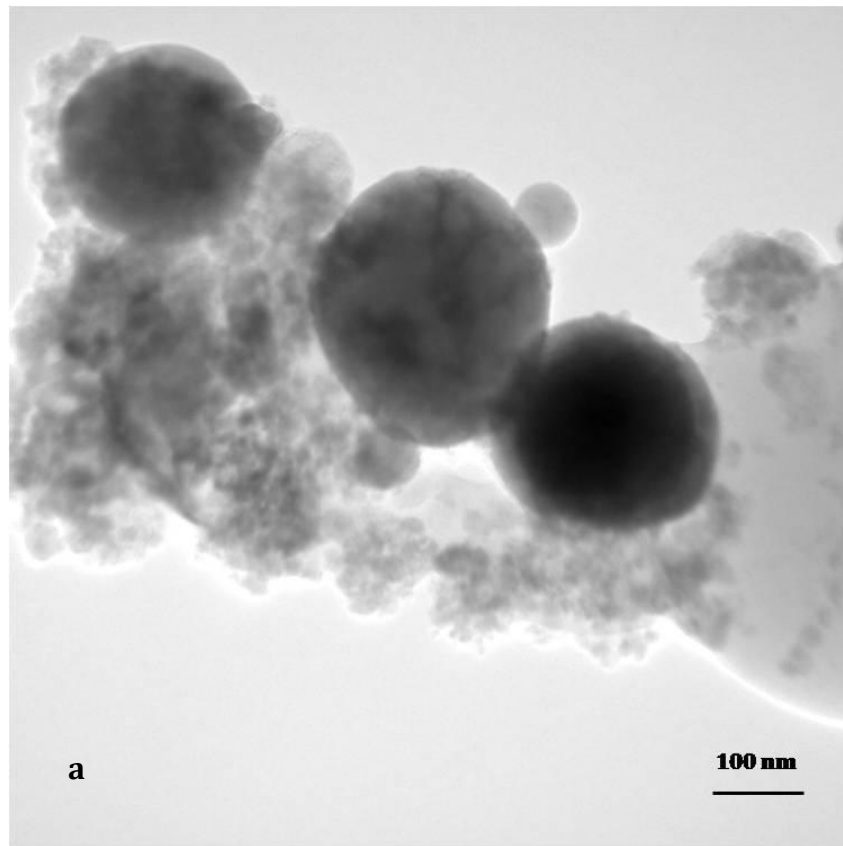


Figure 4.4.9a: Image of a W-Ni-Fe rod penetration aggregate. Original magnification: 20.0kx.

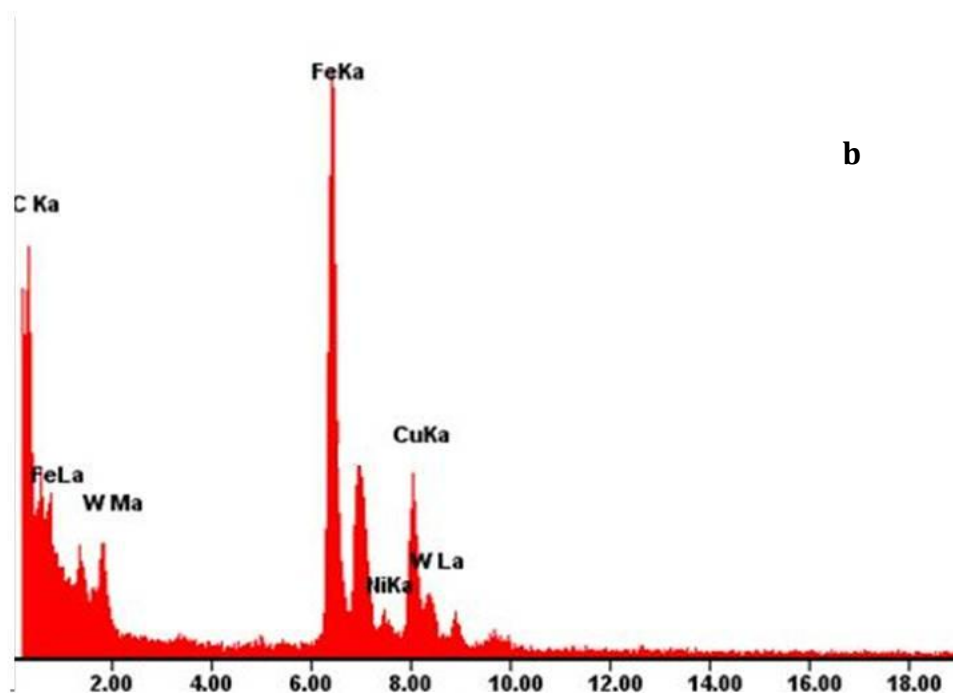


Figure 4.4.9b: EDS spectrum corresponding to Figure 4.4.9a showing a small Ni peak as well as the Cu peak from the TEM grid.

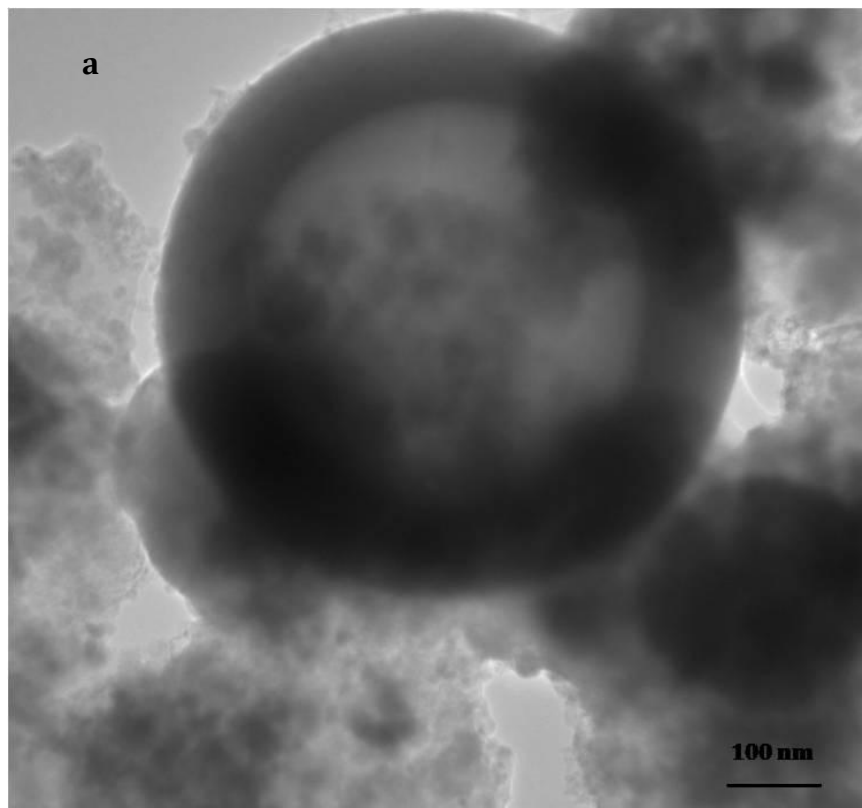


Figure 4.4.10a: Bright-field image of a W-Ni-Co projectile firing.
Original magnification: 20.0kx.

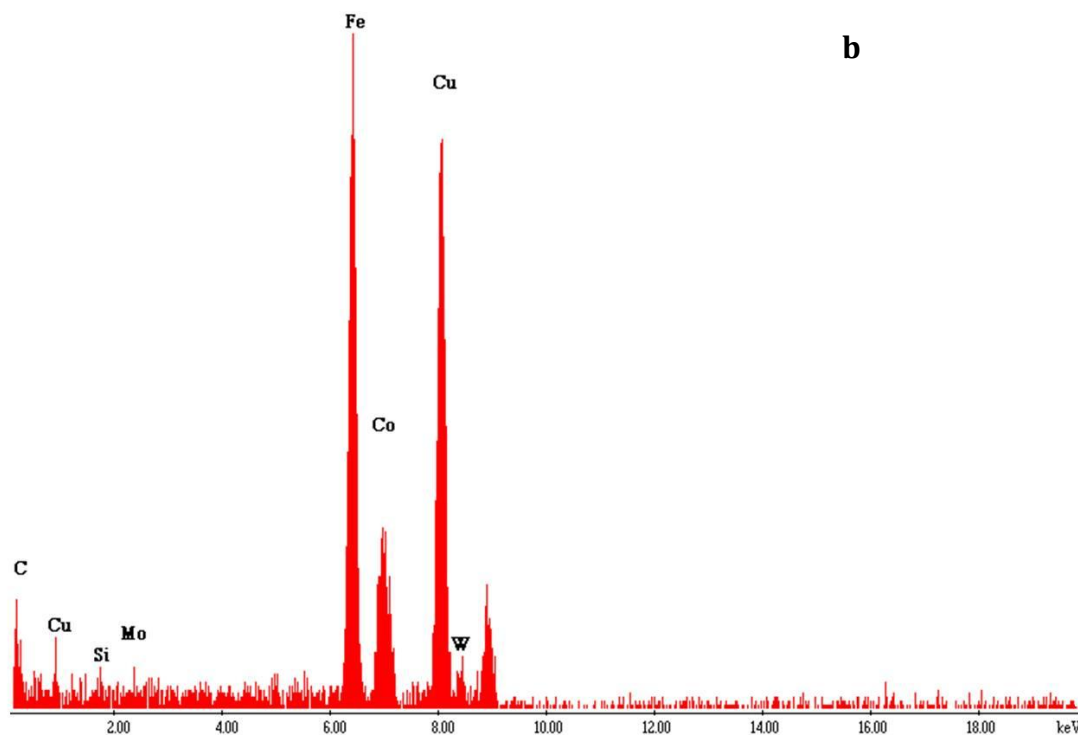


Figure 4.4.10b: EDS spectrum showing a Co peak as well as a Si peak.

In earlier analyses of aerosolized particulates produced by KEP penetrator rods in the open air, there was a higher propensity for W and less for Fe. The percent for Ni in some cases was even fewer than that of Fe [5]. The cascade impactor collector filters were used in these analyses. The SEM analyses showed prominent W fragments which were not observed in this study. Gold also observes spherical particles; they are proposed to result either by “burning in air, splash, and possibly vaporization followed condensation”. Pizaña et al. [19] also show some evidence for the projectile and target melting. The melting would not be the dominant event in the formation of these particles. Their formation is

more attributed to DRX and the formation of equilibrium spherical shapes from erosion products.

The previous study by Gold [5] represents collected particulate sampling greater in size than the size range (from ≈ 5 nm to ≈ 50 nm) characteristic of this study. The ultra-fine or nanoparticulates account for the most significant fraction of aerosol particulate abundance which is equivalent to approximately 90% (number/m³). This corresponds to < 1.5 to 2 % of the mass abundance ($\mu\text{g}/\text{m}^3$). The ultrafine (nano) particles have also been observed in transient mode for diesel engine exhausts [35] as well as in many other samplings of the atmosphere and industrial environments [7, 36, and 37].

4.5 Cytotoxicity Results/Comparison with other Nanoparticulate Examinations

Different publications have demonstrated the health effects of Co, Ni, W, and Fe [38-40]. The exposure to Co, Ni and W can cause pulmonary fibrosis asthma, pulmonary eodema and pneumonia among other effects. Ni compounds in particular have demonstrated to cause nasal and lung cancers for repeated exposure in the long term [39, 40]. A wide range of metal oxides, especially in Fe oxides, have also been confirmed to be toxic or have cytotoxic effects [40, 41]. Figures 4.5.1 to 4.5.4 show the *in-vitro* results for the 48 hrs Viability (MTS) testing of A549 cell cultures for single-stage filter collections and cascade impactor filters (stage 6), respectively. Figure 4.5.1 shows the cell viability results corresponding to single- filter W-Ni-Fe (shot #10) and W-Ni-Co (shot #13). Penetration filters exhibit significant reductions in cell viability or significant increase in cell death in comparison with the two controls, blank filter and media. The blank filter refers to a filter with nothing collected on it. Figure 4.5.2 shows results after 48 hrs incubation/exposure

for the cascade impactor filters. The results in this figure do not show a cytotoxic response for both penetration filters with reference to the controls. The low concentration of particulates in these filters and the type of processing on these filters (Mylar) could have contributed to the non-cytotoxic response. The *in-vitro* results show a slight difference for the W-Ni-Fe and W-Ni-Co in comparison with the *in-vivo* studies where W-Ni-Co fragments were observed to be more toxic [13,14].

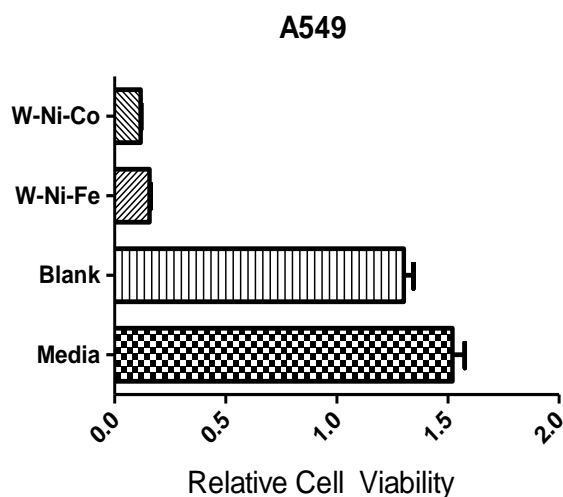


Figure 4.5.1: 48 hrs cytotoxicity results for the single-stage penetration filters in culture assays.

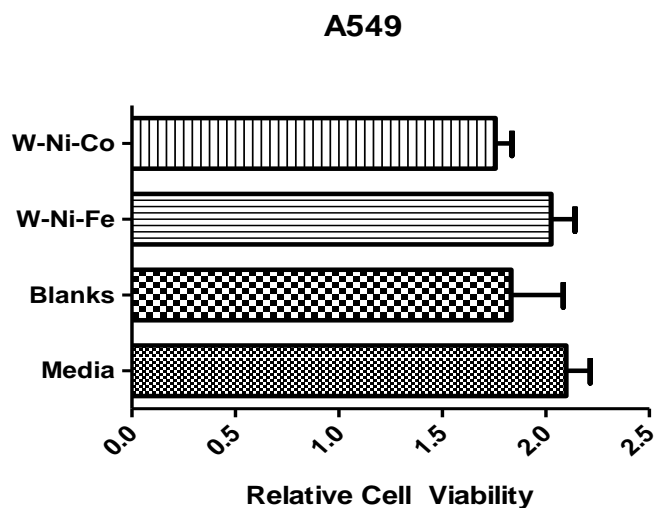


Figure 4.5.2: Cell viability assay for the Mylar filters (Event 3 and 5).

The following figures provide results for two recent cytotoxic assays that were performed for various nanoparticles and are presented for comparison with the cytotoxic assays performed in this study. Figure 4.5.3 shows cytotoxicity *in-vitro* assays for a wide range of nanoparticulates also utilizing the A549 human epithelial cell line [12]. This figure demonstrates varying degrees of cell death for all aggregates of nanoparticulates (PM), however, all are significantly cytotoxic. Figure 4.5.4 shows a direct contact cytotoxicity assay where particulate matter was collected on glass fiber filters and these were layered onto the A549 cells [10]. It can be noted that collected soot material was also quite cytotoxic.

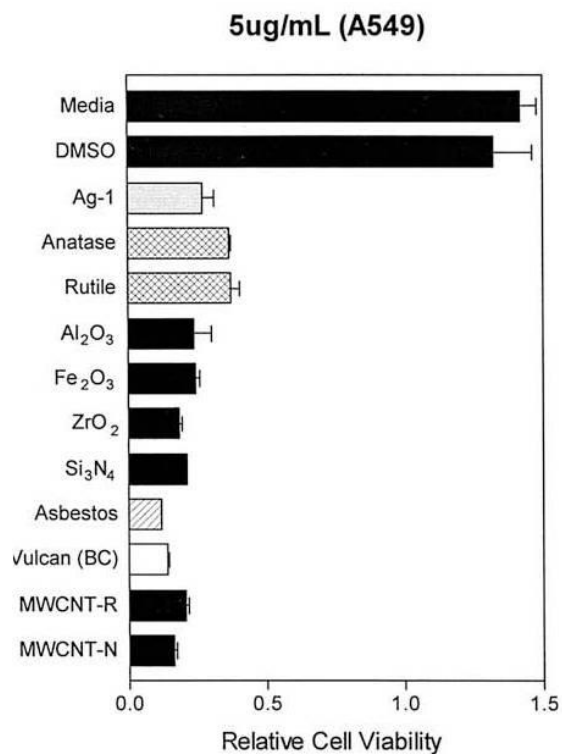


Figure 4.5.3: Cytotoxicity assay results for manufactured nanoparticulate aggregate materials [12].

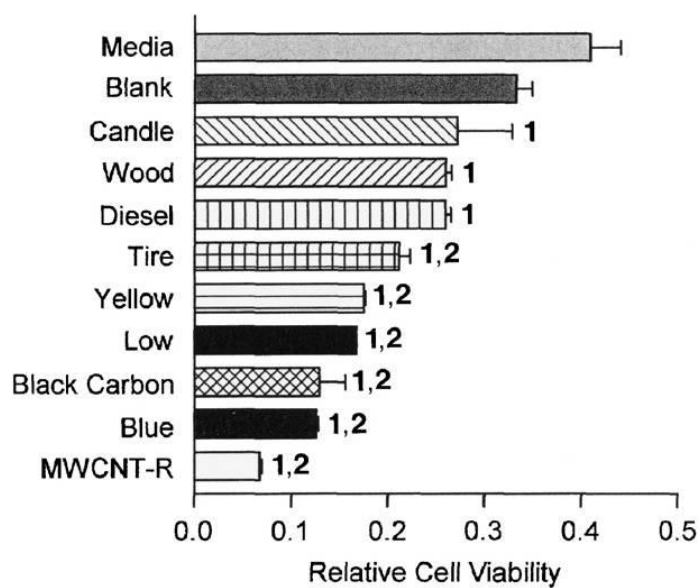


Figure 4.5.4: Direct contact cytotoxicity assay results for human epithelial cells cultures (48 hrs) [10].

In addition to the cell viability assays, concentrations of IL-6 and IL-8 released by A549 cells upon exposure to shots #3 (W-Ni-Fe) and #11 (W-Ni-Co) penetration filters were also determined. The results are shown in Figures 4.5.5 and 4.5.6. It can be observed that IL-6 which acts as a pro-inflammatory and cytokine, is not being induced by the filters when compared to the media and blank controls (refer to Figure 4.5.5). Figure 4.5.6 demonstrates that the filter material inhibits IL-8 production. IL-8 functions as a chemokine, attracting immune cells to the site of injury.

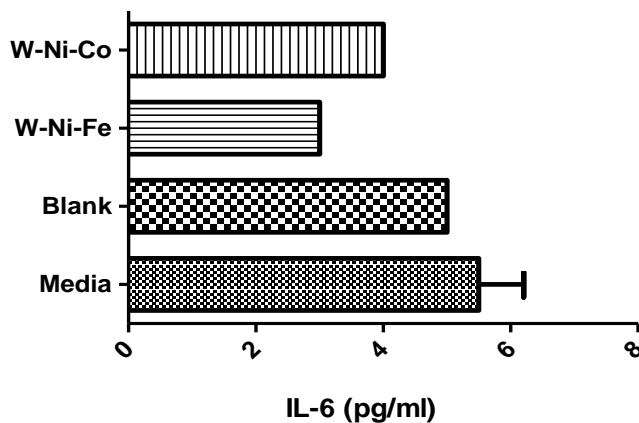


Figure 4.5.5: Cytokine release for two single-stage filters (shots #11 and #3).

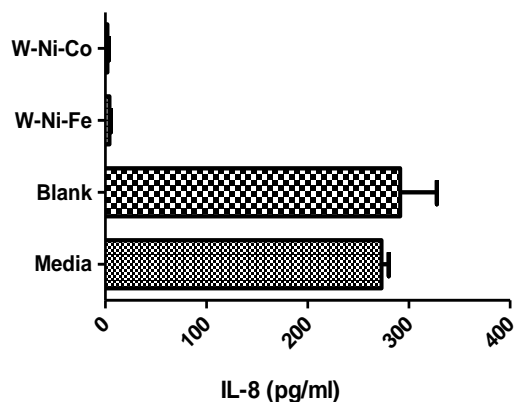


Figure 4.5.6: IL-8 results for the same shots as in Figure 4.5.5.

Since most of these particles are in the inhalable range (nanoparticles $< 1 \mu\text{m}$) they can encounter the mucociliary clearance by cilia of the bronchial epithelial cells which then moves to large particles ($> 1 \mu\text{m}$) towards the upper section of the respiratory tract. Nanoparticles $< 1 \mu\text{m}$ migrate to the alveoli where phagocytes and other cells that also protect the body from harmful foreign particles work to detain them [42]. Particles $< 100 \text{ nm}$ can evade attacks from phagocytes like other pathogens (germs or bacteria) and therefore accumulate to create oxidative stress and inflammation [43]. This accumulation can lead the pathway to other diseases like coronary heart disease, asthma and COPD. High concentrations of aggregated particles can produce pulmonary tissue damage as well as lung burden depending on the clearance rate of the lung [41].

Besides oxidative stress, some nanoparticles can lead to severe inflammation when exposed to viral infections while other nanoparticles can lower the resistance to some types of micro-organisms [44]. This occurrence has been previously described for *in-vitro*

assay for collected aerosol particles on filters where there is IL-8 inhibition; this would prevent an effective response from the lungs to inhaled pathogens. Smaller nanoparticles (< 30 nm) can simulate virus diameters and cross physiological barriers, therefore entering the circulatory lymphatic systems where they can transfer to other organs [45-46]. Studies of oxidative stress in combination with high concentrations of metals such as Cu, Al, and Fe, among others have suggested the promotion of neurodegenerative diseases such as Parkinson's and Alzheimer's diseases [40].

Chapter 5

Summary and Conclusions

5.1 Summary

KE penetrators play an important role in modern-day military armament. KE projectiles made with WHA have been assumed to be relatively benign, but the aerosolized particulates from these WHA projectiles produced during an impact can cause potential long-term health issues similar to DU munitions. Studies of particulate chemistries, size distributions, or cytotoxic responses, especially concerning respiratory health effects has been very limited to some degree. The interaction between the target and the projectile produces micron and submicron-size erosion fragments (aerosolized particulates), as well as reaction product debris from the mechanical mixing between the target and the projectile. Filter collected ballistic aerosol/particulate samplings were examined for two different alloys, W-Ni-Fe and W-Ni-Co. These samplings were collected in two different types of filters, single-stage collector filters and cascade impactor filters. They were characterized using scanning and transmission electron microscopy, elemental composition with energy dispersive spectroscopy, and finally exposed to human epithelial (lung) cells to assess their inflammatory and related respiratory health issues. Furthermore, microstructural analysis was performed on sub-scale WHA rods.

The test assembly used to collect the erosion-created particulates was designed with the assumption that these particulates both from the projectile and the target would create a more representative sampling for the study. In contrast to the SEM analyses where larger

particles were observed, in the TEM analyses ultrafine or nanoparticulates are easier to observe. These types of particulates (nano) account for the most significant fraction of aerosol particulate. Specific TEM analyses on nanoparticle aggregates may represent the rod matrix or matrix components. The particulates microstructural and micro chemical comparisons in SEM and TEM shows very little detectable variation in either chemistry or particle size distributions on the filters.

There is evidence over the last few decades that metal particles and its oxides are toxic for the pulmonary system. Aerosol particulates for the single-stage filter collections (nanoparticulates) exhibited significant cytotoxicity for A549 human epithelial cells. Mylar filters did not reveal any cytotoxicity results. It still can be concluded that various species within the nanoparticulates induce the cytotoxic responses observed in these cytotoxic assays. Current research reviews indicate that the majority (with few exceptions) of nanoparticles and nanoparticle aggregates are toxic and/or cytotoxic to living organisms. However, the connection between nanoparticle exposure and immune response is not yet well known. The degree of toxicity for specific nanoparticles cannot be estimated from materials and their properties which are nontoxic in bulk form, but could be toxic in nanoparticle form.

5.2 Specific Conclusions

- The aerosolized material consisted mostly of small spherical particulates. Individual particles illustrated in the dark-field (TEM) represent mostly W related alloy particulates in the range of 5-20 nm. Individual larger Fe particles from the debris observed in the SEM are larger in size (< 1 nm to ≈ 1 μ m).

- The ratio of respirable particulates to total particulates (mg/m³) collected was similar for W-Ni-Fe and W-Ni-Co, 66% and 69% respectively. 61% of the respirable particulates ($\leq 2 \mu\text{m}$) would originate from the steel target for the W-Ni-Fe projectile penetration and roughly 64% for the W-Ni-Co. The W:Ni ratio was confirmed to be the same in both alloys, approximately 28%.
- Variations in elemental compositions for the different types of filters were observed. SEM/EDS analyses did not detect any Ni or Co at different magnifications. Non-detection of Co and Ni was attributed to its low concentration in the tungsten alloy (total collected aerosol debris was $< 0.01 \text{ wt}\%$) which means that the EDS signal will not detect it because is below the elemental sensitivity of ≈ 0.5 to 1.0% .
- The dominant particulate compositions for all penetration events will be Fe followed by W. It can be observed generally in the majority of the SEM/EDS results that the propensity of the ballistic penetration-related debris and aerosol particulate mass is associated with particle aggregates $> 1 \mu\text{m}$.
- Corresponding EDS results for TEM detected Ni and Co peaks for W-Ni-Fe and W-Ni-Co alloys respectively.
- The particles studied in this project were observed to be cytotoxic after their exposure to human lung cells. In contrast to the single-filters which revealed toxicity in all shots (#3, #11, #10, #13), the Mylar filters did not show the same cytotoxic responses.

- The mass concentration deposited on the Mylar filters was very low in comparison to the single-filters concentration which could be attributed to the position of the impactor stage in relation to the target
- In this study the W-Ni-Fe aerosol particulate collection was slightly more cytotoxic than the W-Ni-Co. In the *in-vivo* studies for much larger (bulk) fragments, the W-Ni-Co was considerably more toxic.

References

- [1] Diarmid, M.A. Mac; Keogh, P.; Hooper H.; et al. 2000. Health Effects of Depleted Uranium on Exposed Gulf War Veterans. *Environ. Res.* 82: 168-180.
- [2] Peimar, T.C.; Ficiarelli, A.F.; Ejnik, S.W.; et al. 1999. Distribution of Uranium in Rats Implanted with Depleted Uranium Pellets. *Toxicol Sci.* 49: 29-39.
- [3] Hain, E.F.; Gilmette R.A.; Hoover M.D. 2002. Implanted Uranium Fragments Cause Soft Tissue Sarcomas in the Muscles of Rats. *Environ. Health Perspect.* 110: 51-59.
- [4] Guilmette, R.A.; Parkhurst, M.A.; Miller, G.; et al. Human Health Risk Assessment of Capstone Depleted Uranium Aerosols: Attachment 3 of Depleted Uranium Aerosol Doses and Risk, Summary of U.S. Assessments, Battelle Press, Columbus, OH. 2006.
- [5] Pope III, C.A.; Dockery, D.W. 2006. Health Effects of Particulate Air Pollution: Lines that Connect. *J. Air & Waste Manage. Assoc.* 56: 709-742.
- [6] Gold, K. Analysis of Aerosols Produced During Tests of Tungsten Alloy Kinetic Energy Penetrators, Technical Report ARWEC-TR-97014, U.S. Army Armament Research, Development and Engineering Center, Picatinny Arsenal, NJ, October, 1997.
- [7] Donaldson, K.; Stone, V.; Clouter, A.; Renwick, L.; Mac Nee. 2001. Ultrafine Particles *Occupat. Environ. Med.* 58: 211-216.
- [8] Oberdörster, G. 2001. Pulmonary Effects of Inhaled Ultrafine Particles. *Int. Arch. Occupat. Environ. Health* 74: 1-8.

- [9] Soto, K.F.; Carrasco, A.; Powell, T.G.; Garza, K.M.; Murr, L.E. 2005. Comparison of *In-vitro* Cytotoxicity Assessment of some Manufactured Nanoparticulate Materials Characterized by Transmission Electron Microscopy. *J. Nanoparticle Res.* 7: 145-169.
- [10] Murr, L.E.; Soto, K.F.; Garza, K.M. 2008. "Chapter 1": Health Hazards of Manufactured, Natural Environmental and Anthropogenic Atmospheric Nanoparticulate Materials: Past, Present and Future. In *Biomaterial and Biomedical Engineering*, ed. W. Ahmed and A. Ali N Al Öchsner, 1-54. Trans Tech Publishers: Switzerland.
- [11] Soto, K.F.; Garza, K.M.; Shi, Y.; Murr, L.E. 2008. Direct Contact Cytotoxicity Arrays for Filter-Collected, Carbonaceous (Dust) Nanoparticulate Material and Observations of Lung Cell Response. *Atmos. Environ.* 42: 1970-1982.
- [12] Murr, L.E. 2008. Microstructures and Nanostructures for Environmental Carbon Nanotubes and Nanoparticulate Soots. *Int. J. Environ. Res. & Public Health.* 5(5): 321-336.
- [13] Murr, L.E.; Garza, K.M. 2009. Natural and Anthropogenic Environmental Nanoparticulates: Their Microstructural Characterization and Respiratory Health Implications. *Atmos. Environ.* 43: 2683-2692.
- [14] Gold, K.; Cheng, Y.S.; Holmes, T.D. 2007. A Quantitative Analysis of Aerosols inside an Armored Vehicle Perforated by a Kinetic Energy Penetrator Containing Tungsten, Nickel, and Cobalt. *Military Med.* 172 (4): 393-398.
- [15] Schuster, B.E.; Demaree, J.D.; Maupin, H.; Kecskes, L.J.; Magness, L.S.; Klutz, B.; Ramirez, D.A.; Murr, L.E.; Russell, L.E. 2008. Metallographic Analysis of Tungsten and Tungsten Alloys Following Implantation in Rat Muscle. *Metal Powder*

- Industries Intl. Conf. on Tungsten Refractory and Handmetals Proceedings, Washington, DC.
- [16] Kalinich, F.; Emand, C.A.; Dalton, T.K.; et al. 2005. Embedded Weapons-Grade Tungsten Alloy Shrapnel Rapidly Induces Metastatic High-Grade Rhabdomyosarcomas in F344 Rats. *Environ. Health Perspect.* 113: 729-731.
 - [17] Pappu, S.; Kennedy, C.; Murr, L.E.; Magness, L.S.; Kapoor D. 1999. Microstructure Analysis and Comparison of Tungsten Alloy Rod and [001] Oriented, Columnar-Grained Tungsten Rod Ballistic Penetrators, *Mater. Sci. Eng.* A262: 115-128.
 - [18] Kennedy, C.; Murr, L.E. 2002. Comparison of Tungsten Heavy-Alloy Rod Penetration into Ductile and Hard Metal Targets: Microstructural Analysis and Computer Simulations. *Mater. Sci. Eng.* A325: 131-143.
 - [19] Pappu, S.; Sen, S.; Murr, L.E.; Kapoor, D.; Magness, L.S. 2001. Deformation Twins in Oriented, Columnar-Grained Tungsten Rod Ballistic Penetrators. *Mater. Sci. Eng.* 2001; A298: 144-157.
 - [20] Pizaña, C.; Murr, L.E.; Baquera, M.T.; Anchondo, I.A.; Putrevu, A.; Piña C.Y.; Tamoria, T.L.; Chen H.C.; Cytron, S.T. 2006. Solid-State Flow, Mechanical Alloying, and Melt-Related Phenomena for [001], Single-Crystal W Ballistic Rod Penetrators Interacting with Steel Targets. *Mater. Sci. Eng.* A428: 301-313.
 - [21] Murr, L.E.; Pizaña, C. 2007. Dynamic Recrystallization: The Dynamic Deformation Regime. *Metall. & Mater. Trans.* 38A: 2611-2628.
 - [22] Trillo, E. A.; Esquivel, E.V.; Murr, L.E.; Magness, L.S. 2002. Dynamic Recrystallization Induced Flow Phenomena in Tungsten-Tantalum (4%) [001] Single-Crystal Rod Ballistic Penetrators. *Matls. Charac.* 48: 407-421.

- [23] Murr, L.E.; Trillo, E.A.; Pappu, S.; Kennedy, C. 2002. Adiabatic Shear Bands and Examples of Their Role in Severe Plastic Deformation. *Journal of Matls. Sci.* 37: 3337-3360.
- [24] Sanchez, Juan C. 1996. M. S. Thesis, The University of Texas at El Paso.
- [25] Carleone, J. 1993. Tactical Missile Warheads: Progress in Astronautics and Aeronautics, edited by J. Carleone. Vol. 155 of American Institute of Aeronautics and Astronautics, Inc, Washington, DC.
- [26] Kennedy, Christine. 2000. Ballistic Perforation of OFHC Cu and 7039 Al Targets: A Microstructural and Hydrocode Study, *Materials Research*. PhD diss., The University of Texas at El Paso.
- [27] Murr, L. E.; Ferreyra, E.; Pappu, S.; Garcia E. P.; Sanchez, J. C.; Huang, W.; Rivas, J. M.; Kennedy, C.; Ayala, A.; Niuo, C.-S. Novel Deformation Processes and Microstructures Involving Ballistic Penetrator Formation and Hypervelocity Impact and Penetration Phenomena. *Matls. Charac.* 37: 245-276.
- [28] Hetland, R.B.; Refsnes, M.; Myran, T.; Johansen, B.V.; Uthus, N.; Schwartz, P.E. 2000. Mineral and/or Metal Content and Critical Determinants of Particle-Induced Release of IL-6 and IL-8 from A549 cells. *J. Toxicol. Environ. Health.* A60: 47-65.
- [29] Hetland, R.B.; Casser, F.R.; Refsnes, M.; Schwartz, P.E.; Lag, M.; Boere, A.F.G.; et al. 2004. Release of Inflammatory Cytokines, Cell Toxicity and Apoptosis in Epithelial Lung Cells after Exposure to Ambient Air Particles of Different Size Fractions. *Toxicol. In Vitro.* 18: 203-212.

- [30] Nelson, S.I., and Martin, T.R. 2000. *Cytokines in Pulmonary Disease: Infection and Inflammation Lung Biology in Health and Disease*. New York: Marcel Dekker Inc.
- [31] Van Eeden, S.F.; Tan, W.C.; Suwa, T.; Fujji, T.; et al. 2001. Cytokines Involved in Systemic Inflammatory Response Induced by Exposure to Particulate Matter Air Pollutants (PM10). *Amer. J. Respir. Crit. Care Med.* 164: 826-830.
- [32] Chung, K.F. 2001. Cytokines in Chronic Obstructive Pulmonary Disease. *Environ. Respir. J.* 18: 505-595.
- [33] Holgate, S.T., and Busse, W.W. BUSSE, eds. 1998. *Inflammatory Mechanisms in Asthma*. New York: Marcel Dekker, Inc.
- [34] Barnes, P.; Drazen, J.; Rennard, S., and Thomson, N. eds. 2008. *Asthma and COPD*. New York: Academic Press.
- [35] Murr, L.E. 1972. Fossilization of Electrical Corona Streamers from Silicon Nitride Crystals in the Electron Microscope. *Popular Magazine*, March.
- [36] Abdul-Khalek, I.S.; Kittelson, D.B.; Graskow, B.R.; Wei Q.; Brear, F. 1998. *Diesel Exhaust Particle Size: Measurement Issues and Trends*. Pennsylvania: Soc. Automotive Engineers.
- [37] Hughes, L.S.; Cass, G.R.; Jones, J.; Awes, M.; Olmec, L. OLMEC. 1998. Physical and Chemical Characterization of Atmospheric Ultrafine Particles in the Los Angeles Area. *Environ. Sci. Technol.* 33:113-1161.
- [38] Murr, L.E.; Soto, K.F.; Garza, K.M.; Guerrero, P.A.; Martinez, F.; Esquivel, E.V.; Ramirez, D.A.; Shi, Y.; Bang, J.J.; Venzor, J. 2006. Combustion Generated Nanoparticulates in the El Paso, TX, USA/Juarez, Mexico Metroplex: Their

- Comparative Characterization and Potential for Adverse Health Effects. *Int. J. Environ. Res. Public Health*. 3(1): 48-66.
- [39] Cugell, D.W.; Morgan, W.K.C.; Perkins, A. 1990. The Respiratory Effects of Cobalt. *Arch. Internal Med.* 150 (1): 177-183.
- [40] Sullivan, S.B.; Kviezar, Jr. C.R. eds. 2001. *Clinical Environmental Health and Toxic Exposure*, 2nd edition. Philadelphia: Lippincott Williams & Wilkins.
- [41] Buzca, C.; Pacheco, J.; Robbie, K. 2007. Nanomaterials and Nanoparticles: Sources and Toxicity. *Biointerphases*. 2: MR17-71.
- [42] Murr, L.E.; Soto, K.F.; Garza, K.M. 2008. Chapter 1: Health Hazards of Manufactured, Natural Environmental, and other Anthropogenic Atmospheric Nanoparticulate Materials: Past, Present and Future. *In Biomaterials and Biomedical Engineering*, ed. W Ahmed, N Ali and A. Ochsner, 1-55. Switzerland: Trans. Tech. Publishing.
- [43] Oberdorster, G.; Ferin, J.; Lehnert, B.E. 1994. Correlation between Particle Size, *In-Vivo* Particle Persistence, and Lung Injury. *Environ Health Perspect* 102: 173-179.
- [44] Mayer, Gene. 2008. Immunology-Chapter 1: Innate Immunity. *Microbiology and Immunology On-Line Textbook*, <http://pathmicro.med.sc.edu/ghaffar/innate.htm> (accessed on October 21, 2009).
- [45] Dobravolvkaia, M.A.; McNeil, S.E. 2007. Immunological Properties of Engineered Nanomaterials. *Nature Nanotechnol.* 2: 469-478.
- [46] Sonavane, G.; Tomoda, K.; Makino, K. 2008. Biodistribution of Colloidal Gold Nanoparticles after Intravenous Administration: Effect of Particle Size. *Colloid Surf. B. Biointerphases*. 66: 274-280.

Curriculum Vita

Brenda Machado was born on February 22, 1984 in Cd. Juarez, Chihuahua, Mexico. The only child of Jose Luis Machado and Gabriela Lopez. She graduated from Jefferson High School in El Paso, TX, in 2002. She received her Bachelor of Science degree in Metallurgical and Materials Engineering in 2007 from the University of Texas at El Paso (UTEP) and later entered the Graduate School at UTEP to complete her Master of Science (M.S.) degree in Metallurgical and Materials Engineering in December of 2009.

Permanent address: 337 Barcelona Dr.

El Paso, TX, 79905

This thesis was typed by Brenda Machado.